MASTERARBEIT | MASTER'S THESIS

Titel | Title

Light dark matter detection using repetitive non-destructive readout DePFETs

verfasst von | submitted by

Niels Frederik Tim Wernicke BSc

angestrebter akademischer Grad | in partial fulfilment of the requirements for the degree of

Master of Science (MSc)

Wien | Vienna, 2024

Studienkennzahl lt. Studienblatt | Degree programme code as it appears on the student record sheet:	UA 066 876
Studienrichtung lt. Studienblatt | Degree programme as it appears on the student record sheet:	Masterstudium Physics
Betreut von | Supervisor:	Dipl.-Ing. Dr. Wolfgang Waltenberger Privatdoz.

Zusammenfassung

Die Suche nach Dunkler Materie konzentrierte sich in den letzten Jahrzehnten weitgehend auf *weakly interacting massive particles* (WIMPs), das heißt Dunkle Materie mit einer Masse die schwerer als ein Proton ist oder oberhalb von $1\ \mathrm{GeV}/c^2$. Diese Annahme wurde unter anderem durch die sogenannte Lee-Weinberg bound für schwach wechselwirkende Teilchen und potenzielle Synergien von derartigen Dunkle Materie Kandidaten mit Supersymmetrischen Teilchen motiviert. Aufgrund der ausbleibenden Entdeckungen dieser Teilchen in Beschleunigerexperimenten sowie von WIMPs in Experimenten zum direkten Nachweis Dunkler Materie erlangten Modelle für leichte Dunkle Materie zunehmend Bedeutung. Mit Hilfe von *repetitive non-destructive readout* (RNDR) *depleted p-channel field effect transistor*s (DePFETs) wird im DANAE Experiment versucht, diese leichte Dunkle Materie direkt nachzuweisen. Da deren Masse nicht groß genug ist, um messbare Signale in einem Streuprozess mit Atomkernen zu verursachen, werden Elektronenrückstöße studiert. Aufgrund des geringen Dunkelstroms, der hohen Sensordicke und der Möglichkeit, Signale von wenigen Elektronen aufzulösen, sind RNDR DePFETs für diese Anwendung prädestiniert. Da diese Sensoren aus aktivem Pixel bestehen, können eine Vielzahl an Pixel parallel ausgelesen werden. Das Rauschen wird verringert, indem die Ladung in jedem Pixel zerstörungsfrei wiederholt ausgelesen und gemittelt wird. In dieser Masterarbeit soll die Sensitivität des Experiments verbessert, und Daten analysiert werden.

Nachdem der Aufbau des Experiments optimiert wurde, um einen besseren Betrieb zu ermöglichen, wurden die Betriebsparameter angepasst. Der Detektor wird mit einer Sequenz gesteuert, welche die Länge und Abfolge der einzelnen Ausleseschritte bestimmten. Diese wurde modifiziert, um die Expositionszeit des Detektors zu steuern und die Auslese, unter anderem um eine konstante Belichtung aller Pixel zu ermöglichen. Nachdem ein weiterer Detektor aufgebaut und in das Setup integriert wurde, mussten Fehler identifiziert und behoben werden. Im Zuge dessen, wurden Bauteile für zukünftige Anpassungen des Setups mit den Technickern vom HEPHY geplant und erstellt. Der Betrieb des Detektors ermöglichte die Aufnahme von Messreihen unter verschiedenen Bedingungen – wie Temperatur und Belichtungszeit – die schlussendlich ausgewertet und analysiert wurden.

Die Auswertung ergab eine Generationsrate von 0,02 Elektronen pro Sekunde und Pixel bei einer Temperatur von $110\ \mathrm{K}$. Für Temperaturen unterhalb von $110\ \mathrm{K}$ müssen die Messmethoden und der Betrieb des Detektors angepasst werden, damit die Identifikation von Ereignissen weiterhin zuverlässig funktioniert.

Abstract

Within the last decades, the search for dark matter largely focused on *weakly interacting massive particles* (WIMPs), or dark matter candidates with a mass greater than a proton or heavier than $1\ \mathrm{GeV}/c^2$. This approach was mainly motivated by the Lee-Weinberg bound for weak interacting particles as well as potential synergies with super-symmetric models. Due to the lack of discoveries of such particles combined with the increasing size of the excluded parameter space by direct dark matter detection experiments, models of light dark matter increasingly gained importance. Using *repetitive non-destructive readout* (RNDR) *depleted p-channel field effect transistor*s (DePFETs), the DANAE experiment aims to detect light dark matter. Due to their light masses, the scattering process on atomic nuclei will not result in a measurable signal and the interaction between dark matter candidates and electrons needs to be studied. The specific properties of RNDR DePFETs, such as a thick fully depleted silicon bulk, a low dark current and the capability to resolve the signal of single electrons made it an ideal option for this application. In DePFET detectors, a great number of pixels can be read out in parallel. The noise is reduced by repeatedly and non-destructively reading out individual pixels. This master thesis aims to improve the sensitivity of the experiment and analyse data.

The experimental setup was optimized to improve the operation. The detector is controlled by a sequence that determines the duration of the readout steps. This sequence was modified to change the exposure of the detector to achieve a constant exposure time for all pixels. After assembling and installing a new detector, several errors were identified and corrected. The differences in the operation between both detectors were analysed. Additionally, components for future configurations were developed and built together with technicians of the HEPHY. A measurement series with varying temperature and exposure times was performed to acqurie data and analyse them with specific software packages.

The analysis resulted in the determination of a generation rate of 0.02 electrons per unit time and pixel at a temperature of $110\ \mathrm{K}$.For temperatures below $110\ \mathrm{K}$, the operation of the detector needs to be adjusted to ensure a proper event identification.

Contents

Page

I. Theoretical background 1

1. Introduction 1

2. Does dark matter exist, and what is it? 3
2.1. Evidence of dark matter . . . 3
2.2. Properties of dark matter . . . 6
2.3. Types of dark matter . . . 7

3. How dark matter is detected 9
3.1. Scintillation . . . 9
3.2. Phonons . . . 10
3.3. Electron scattering and ionisation . . . 10

4. Detection Methods 12
4.1. Semiconductors . . . 12
4.2. Detection . . . 14
4.3. DePFET detectors . . . 16
4.4. RNDR DePFET detectors . . . 17

5. Noise 18
5.1. General kinds of noise . . . 18
5.2. Dark current . . . 19
5.3. Noise in DePFET detectors . . . 19

II. The experimental setup 22

6. The setup of the DANAE experiment 22
6.1. General setup of DANAE . . . 22
6.2. The readout board . . . 23
6.3. Characteristics of the detector . . . 25
6.4. Supply Voltages . . . 26

7. Operation of the Detector 28
7.1. The pattern sheet . . . 28
7.2. The instruction sheet . . . 28
7.3. Output . . . 30

8. Improvement of the operation sequence 31
8.1. Exposure time . . . 31
8.2. Line wise clearing of the detector . . . 32

9. Design of new and improved parts 33
9.1. Improving the shielding . . . 33
9.2. Redesign of the frame for the readout board . . . 33

9.3. New design of the frame . . . 34
9.4. Redesign of the outer shielding for the new setups . . . 35

10. Installation of the new detector **36**
10.1. The components . . . 36
10.2. Troubleshooting . . . 37

III. Results **38**

11. Analysis of the data with ROAn **38**
11.1. Composition of the data and first quality control . . . 38
11.2. Offset correction . . . 39
11.3. Common mode correction . . . 39
11.4. Slopes of the RNDR readout . . . 40
11.5. Noise map . . . 40
11.6. Event map . . . 41
11.7. Event tree . . . 42
11.8. Gain map . . . 42

12. Results from a temperature and exposure sweep **44**
12.1. Selection and correction of the data . . . 45
12.2. Number of events . . . 47
12.3. Events per unit time . . . 48
12.4. Offset . . . 49
12.5. Further interpretation using pixel-wise analysis . . . 50
12.6. Discussion . . . 51

13. Future prospects for DANAE **54**
13.1. Shielding . . . 54
13.2. Sensitive Mass . . . 54
13.3. Fine tuning . . . 55

14. Conclusion **56**

List of Acronyms **57**

References **58**

Part I: Theoretical background

1. Introduction

According to theories explaining the observations of the movement and distribution of matter in the universe, about 80% of its mass content is dark matter. While the theories explain the makeup of the universe, no direct measurements have confirmed those theories. The quest to prove or disprove the existence of dark matter is one of the most important and most pressing research fields in modern physics.

While there have been several direct detection experiments for dark matter, almost all have turned up empty so far [1]. Most of these experiments are set up to find WIMPs, while the search for light dark matter is less frequently elaborated. Light dark matter detection experiments investigate event signatures of electron recoils. For this reason, a low, deep sub-electron noise is required to achieve a sensitivity on single electrons. In recent years silicon was established as a powerful combination of target and sensing material especially by using skipper CCDs. However, this technology is affected by long readout times, in the order of hours. For this reason, the DANAE experiment aims to establish *repetitive non-destructive readout* (RNDR) *depleted p-channel field effect transistor*s (DePFETs) as an alternative, active pixel technology. The experiment is located at HEPHY and operated by the ÖAW and is searching for evidence of light dark matter.

The major challenge for the detection of dark matter is the weak interaction – regarding the strength not the fundamental force – between dark and ordinary, baryonic matter. Beside gravity, most models assume additional forces like electroweak interaction. In the context of experimental physics, these parameters are covered by an effective cross section of the particle. As a consequence, very sensitive detectors are needed to achieve a sufficient signal-to-noise ratio. This can be facilitated by reducing the noise of the measurement or by increasing the signal with exceptional large detector masses.

The first experiments to detect light dark matter were realized with comparable small masses, due to the increased particle flux compared to WIMPs. The total mass density of dark matter at the position of the earth can be predicted. It is about $\rho_{DM=}390\,\mathrm{MeV}/c^2\mathrm{cm}^3$ [1]. This density is the same, regardless of the type and mass of the assumed dark matter. However, due to the smaller mass of the individual particles of light dark matter compared to WIMPs, the number of particles per volume is much higher. As a consequence, a signal with statistical relevance of light dark matter is achievable by much smaller detectors, compared to classical dark matter experiments.

DANAE employs RNDR DePFET detectors due to their sub-electron noise for direct light dark matter searches. DePFETs were developed for astronomical purposes, like the detection of x-rays in the satellite mission ATHENA to benefit from their high SNR and time resolution. They are also used in particle colliders like BELLE and in future perhaps ILC [2].

The aim of this thesis is to improve the setup of DANAE, collect data and analyse them. This leads to a characterization of the current performance and the identification of future modifications. Parts of the experimental set-up were optimized to streamline the opera-

[1] Excluding the DAMA/LIBRA experiments, whose results are still under discussion because of a failing certification and limited access to the data.

tion of the experiment. Current and future goals were considered for this optimization, including the temperature shielding and extension and debugging of electronics.

A new detector module was installed and commissioned by debugging problems, which are documented for future reference. In future configurations multiple sensors will be operated in parallel to increase the sensitivity of the experiment. In this context, the operation sequence sent to the detector was improved. The I^2C commands to active integrated circuits of the setup must be understood and adjusted to verify a proper operation. Other improvements of the sequence resulted in a flexible controllable exposure time, homogeneously distributed between all pixels. In a mechanical context, 3D models have been created for the altered parts. For this the handling of "FreeCAD" and "Autodesk Inventor" were learned. Both are programs to create CADs. Many changes had to be made in close collaboration with the technicians of HEPHY.

Within a literature review of the first part, evidence for the existence of dark matter is provided, and its properties are discussed. Different detection methods for direct experiments are reviewed, before explaining the function and operation of DePFETs, as well as the method to reduce and control its noise.

The second part explores the setup of DANAE, describing the physical experiment components and the operation of the detector. It includes the operational improvements of the experiment, done within this thesis. Subsequently, a proposal for new and improved parts are presented, as well as the installation of the new detector.

The third part is about the analysis of the data collected during DANAE. First the software program ROAn is discussed before focusing on the generated results and possible improvements stemming from these.

Lastly, future plans for DANAE are presented. They aim to improve the sensitivity of the experiment by minimising errors and noise from outside sources. Especially, different detector configurations aim to further increase the sensitivity of the setup.

2. Does dark matter exist, and what is it?

2.1. Evidence of dark matter

The Evidence for dark matter is provided by astronomical observation. The following three sections focus on selected observations at very different orders of magnitude. As a consequence, a negation of the effects would require mechanisms that display a similar effect at very different scales. This concerns the movement of galaxy arms (paragraph 2.1), which size ranges at the order of tens of kilo parsec. Another observation is the collisions of galaxy clusters (paragraph 2.1), which are in the size range of mega parsec. Final evidence for dark matter is the *cosmic microwave background* (CMB) (paragraph 2.1), which includes all the observable universe.

Galaxy arms movement

Thanks to Kepler's Laws, the velocity of objects v can be calculated using the gravitational constant G and the distance r from a central body with mass m. To hold more generally, the mass profile $m(r)$ is used instead of a point mass.

$$v = \sqrt{\frac{G\, m(r)}{r}} \tag{1}$$

The velocity, of the orbiting bodies decreases quadratically with the distance from the central body, and the angular velocity ω decreases with $\omega = \frac{v}{r}$.

The measured velocity v_{circ} of the stars orbiting the galaxy does not decrease significantly, instead it levels out (Fig. 1). This is not congruent with only the gravitational effects of baryonic matter. Baryonic matter meaning the well understood particles from the standard model of particle physics. The presence of dark matter explains the observed velocities. The dark matter is assumed to be dispersed around the galaxy in the form of a halo [3]. More general, by assuming an equipartition of kinetic energy, the viral theorem proposes a total mass much higher than the observed one [4].

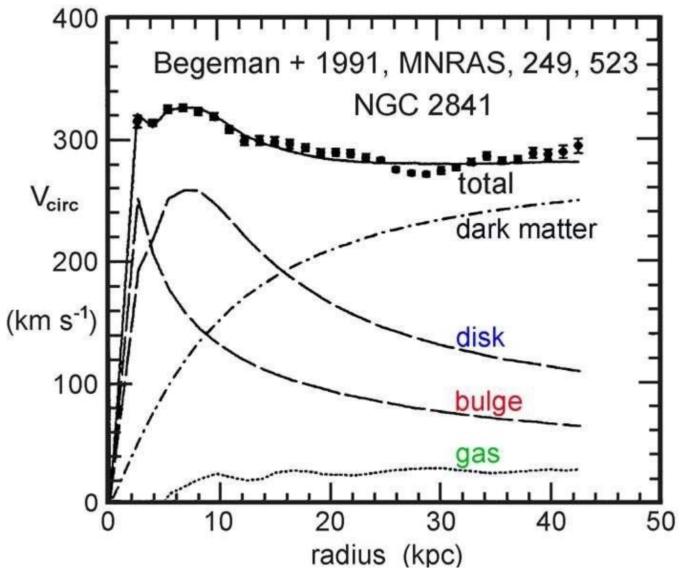

Fig. 1: The black points are the measurements of the rotational speed, including the uncertainties. Adapted from [5].

Galaxy cluster collisions

Clusters of galaxies are hundreds or thousands of gravitationally bound galaxies. The collisions of such clusters have been observed and analysed.

The best-known example for a collision is the Bullet Cluster, or 1E 0657-558. It is made up of two separate galaxy clusters, that collided about 100 million years ago. During the collision, the galaxies passed each other without the individual stars crashing into each other. Meanwhile, the plasma of the clusters experienced ram pressure. This resulted in a heat up of the plasma and x-rays emission. This process slows the plasma down, to the point of being left behind by the galaxies [6].

The baryonic matter mass distribution of a galaxy cluster is about 75% plasma and 25% star mass [7]. At the same time, the gravitational potential of the cluster was investigated by making use of gravitational lensing. The mass of the baryonic matter is concentrated in the middle of the collision, in the form of plasma. However, the gravitational lensing locates a significant mass in the periphery, in which only a quarter of the baryonic mass is located (Fig. 2). This gives a strong indication to invisible matter that interacts weakly with itself, and ordinary matter [6].

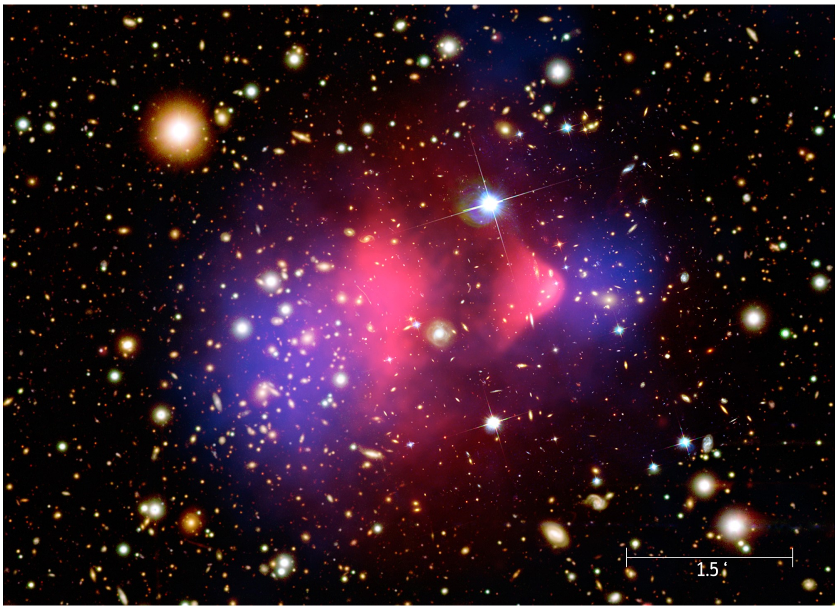

Fig. 2: The Bullet Cluster. Emitted x-rays are shown in red and the intensity of gravitational lensing in blue. The stars are displayed in the visible spectrum [8].

This phenomenon has been observed in other galaxy cluster collisions as well. According to David Harvey et al. 72 collisions have been observed, that prove the existence of dark matter with a significance of 7.6σ [9].

The discrepancy between the observed gravitational effects and the predicted effects with only baryonic matter, could be explained with alternative gravitational theories such as *modified newtonian dynamics* (MOND).

However, these theories do not explain the differing observations before and after the collisions. While both the prior state and the final state in and of itself could be explained with some form of MOND, the transition between those states cannot described with MOND (Fig. 3). [10]

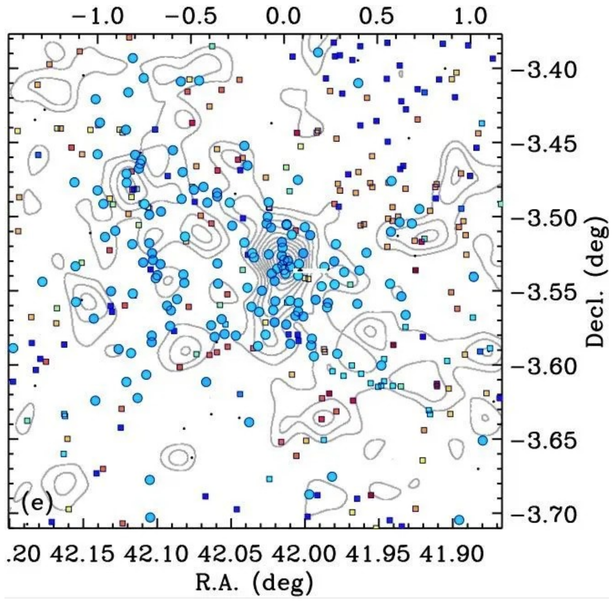

Fig. 3: The dots are stars in the cluster, the squares are stars outside the cluster. The grey lines represent the weak-lensing map of the galaxy. From [10]

Cosmic Microwave Background

According to the actual model of the universe, the *cosmic microwave background* (CMB) radiation was emitted immediately after the Big Bang, during the recombination. The matter of the universe was hot plasma for roughly the first $380\,000$ years. This plasma was opaque, meaning it absorbed all light emitted after relatively short distances.

Because of its expansion, the universe cooled down to about $3000\,\mathrm{K}$ after $380\,000$ years. After the plasma became cold enough, the protons and electrons combined to form neutral hydrogen. The electrons first bound in a high energy state, but quickly released the excess energy in form of radiation. The so formed hydrogen is transparent and released light was not reabsorbed. During further expansion, the light was red-shifted, and formed the CMB, which is the oldest light detectable [11].

While the CMB is the best example measured for black body radiation, there are still thermal fluctuations at the order of $10\,\mu\mathrm{K}$. The power spectrum corresponds to a Fourier transformation in spherical coordinates. The power spectrum of the CMB is shown in Fig. 4. The temperature fluctuations are plotted against the spherical harmonic modes, which are correlated with an angular scale. The power of the power spectrum shows how smooth the temperature map of the CMB is in the size range of the angular scale.

The distribution can be compared to the sea with its big waves on a stormy day. At large scales, the sea is flat. When taking a blurry picture from far away, there are no valleys and mountains of water. When the picture however is taken from the beach, the waves are visible with their ups and downs. On the scale of a meter, the sea is not smooth, but very rough indeed. However, this changes again, when looking at very small scales. A picture taken with a macro-objective, where only a centimetre is visible, is smooth again. Each individual picture taken at such a scale shows smooth water, with maybe an extremum somewhere in the picture, and smoothness everywhere else.

The same principle is used for the CMB. When looking at the CMB, the size of the fluctuations is mostly in the size range of $1°$, while it is smooth for larger and much smaller areas (Fig. 4) [13].

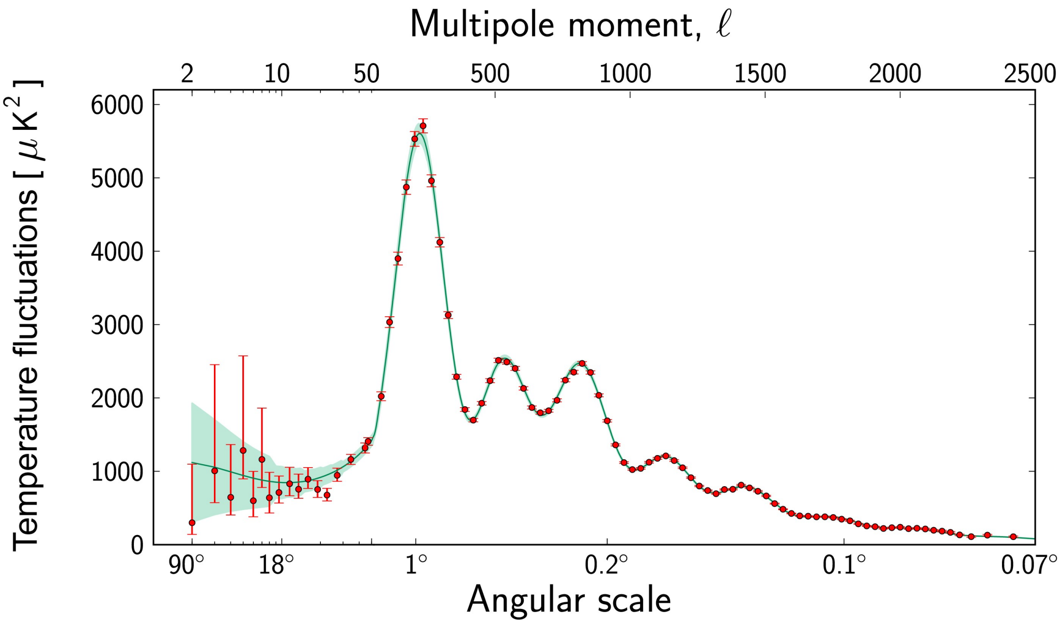

Fig. 4: The temperature fluctuations in the CMB, as measured by the Plank satellite. The fluctuations are plotted against the angular scale, respectively the spherical harmonic modes l [12].

At the large-scale fluctuation appear with $l \leq 30$ and fluctuation plateaus at a low level. This is due to the Sachs-Wolfe effect and corresponds to dark energy in the universe. At small angular scales, there are damping effects because of the increase in the mean free path of the photons [14]. The middle phase shows an oscillation. Those are due to the fluctuations in the local density of the baryons and photons. At some points, the matter density was higher, creating outward electro-magnetic pressure. Due to the higher density, the matter did not significantly cooled down. This pressure works against the local increase in pressure, thwarting its formation and a fluctuation arose [13].

The matter needed to generate these fluctuations congruent with the observed power spectrum and can be calculated. However, this shows, that much more mass is needed, then the one indicated by the visible matter in the universe. Thus, the assumption of dark matter can explain these observations [13].

2.2. Properties of dark matter

In order to efficiently explain all observations of dark matter (including those of section 2.1), certain properties are proposed:

Velocity

Dark Matter shall be non-relativistic, meaning it must be made up of massive particles. If this were not the case, dark matter would not accumulate enough to form gravitational wells. This is called cold dark matter [15].

Stability

Dark Matter shall be stable enough to still exist today. This means the half live of dark matter has to exceed the lifetime of the universe [15].

Mass range of dark matter

The mass range of dark matter is $(10^{-21} - 10^{58})\,\mathrm{eV}$, the upper limit is about $30\ \mathrm{M}_\odot$, spanning from very light particles to primordial black holes [16].

Density of dark matter

The local density - i.e. the density of dark matter at a distance away from the galactic centre of $(10-20)\,\mathrm{kpc}$ - of dark matter is about $\rho_{darkmatter=}390\,\mathrm{MeV}/c^2\mathrm{cm}^3$. [1] This density is about a million times higher, than the average density in the complete universe.

Dark Matter interaction

Dark Matter, as the name suggest, does not emit light and depending on the model interacts weakly electromagnetically with normal matter. Further, dark matter interacts, if at all, only very weakly with itself [17].

2.3. Types of dark matter

Several candidates were proposed to explain the indirect observations of dark matter. Within a non-exhaustive list models of baryonic dark matter are presented first, followed by more exotic types of matter:

MACHOs

On possible explanation for dark matter, are *massive compact halo object*s (MACHOs). Those are massive, invisible objects, like brown draws, planet size objects or black holes. The black holes would need to be primordial, which means they were created with the Big Bang. Otherwise, there would not have been enough time for them to form.

However, the number of massive objects observed constraints their contribution to dark matter to a small percentage. If they have any contribution at all, it is not a major one [18].

Sterile neutrinos

Sterile neutrinos do not belong into the category of cold dark matter, instead they move at relativistic speeds and are therefore considered hot. As a consequence, not Λ-*cold dark matter* (Λ-CDM) is assumed to explain the universe, but instead Λ-*mixed dark matter* (Λ-MDM), with Λ being the cosmological constant. Another benefit of this candidate is, that it would eliminate anomalies of the neutrino oscillations [19].

WIMPs

The dominant model are *weakly interacting massive particles* (WIMPs). They are assumed to be produced in the freeze out of the universe after the big bang. The mass range for WIMPs is from GeV to TeV [20]. They are considered as very likely candidates for dark matter, and many experiments are trying of find evidence of their existence. Those experiments often use recoil from dark matter-nucleus interaction [21].

Axion

While *quantum chromodynamic* (QCD) is very successful, its Lagrangian can lead to CP-violations. However, CP-violations are not observed. A possible explanation is given by the Peccei-Quinn solution, which leads to small particles called axioms, they have masses of about $10^{-4}\,\mathrm{eV}$ [20].

Light dark matter

An important part of gamma astronomy are $511\,\mathrm{keV}$ rays, that are emitted, when an electron-positron pair annihilates each other. The amount of those events observed is hard to explain. On possible solution is light dark matter. [22]. Similarly to WIMPs, they interact weakly, but their mass is in the range of keV to MeV. Light dark matter will be the focus of this work.

The needed mass density of dark matter calculated from observations does not depend on the type of dark matter. Since the mass of light dark matter is several magnitudes smaller than the mass of WIMPs, the number density is magnitudes larger. For a similar cross section as WIMPs and a sufficient sensitivity, the amount of detected events would therefore be much greater. The sensitive volume therefore can be smaller than for detection of WIMPs.

3. How dark matter is detected

There are many ways to potentially detect dark matter. The method chosen depends greatly on what type of dark matter needs to be detected. They fall broadly into three categories (Fig. 5).

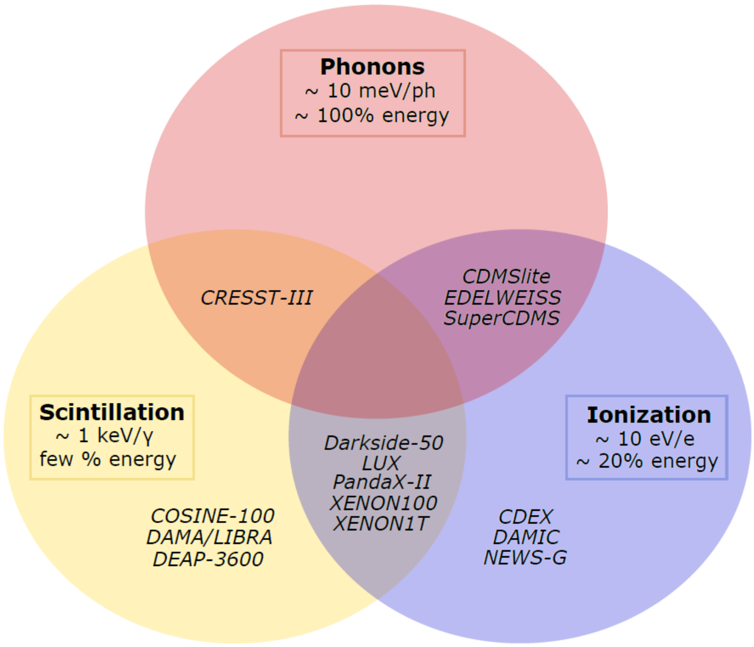

Fig. 5: The three channels for dark matter detection are to detect phonons or the heat generated by the interaction, the scintillation and ionisation of the target. There are example experiments for the different detection channels, with DANAE using ionisation for its detection. Graphic from [23].

The different channels give information about different properties of the dark matter particle that interact. When using scintillation, the energy of the interacting particle can be determined. With nuclear recoil, the nature of the particle can be understood. This way, the signal can be discerned relatively reliably from the background [24].

Electron recoil is affected both by WIMPs and light dark matter detection. The most efficient event signature of massive particles are nuclear recoil. For light dark matter however nuclear recoils cannot generate a significant signal and are neglected, while electron scattering is dominant.

3.1. Scintillation

When dark matter hits some target materials, a photon might be emitted. The energy of the photon depends on the energy of the dark matter and the detector material.

For instance, the *cryogenic observatory for signals seen in next-generation underground searches* (COSINUS) experiments uses natriumiodid crystals for both scintillation and phonon creation. The crystal is cooled to temperatures of a few milli-Kelvin in order to detect small amounts of energy, which heat up the sensitive material with a transition edge sensor. In addition, a light detector is placed around the target crystal to detect the photons generated from scintillation [24].

3.2. Phonons

Nuclear recoil can be used to detect WIMPs with the mass m_χ. They hit the target nucleus, with mass m_T, with galactic speeds. Their kinetic energy corresponding to their velocity is E_χ.

When the dark matter interacts with the target, a maximum recoil energy E_{recoil} is transferred [25]:

$$E_{recoil} \leq E_\chi \frac{4\, m_T\, m_\chi}{(m_T\ +\ m_\chi)^2} \tag{2}$$

For WIMPs with a mass of $100\,\mathrm{GeV}/c^2$ with target mass of $100\,\mathrm{GeV}/c^2$, the recoil energy is at maximum of $50\,\mathrm{keV}$ [25].

The recoil energy can be detected using different methods. In the CRESST experiment, the energy deposited due to interaction with WIMPs increases the temperature. Since super conductors at the edge between their superconducting phase and the normally conducting phase are used, small variations in temperature change the resistance of the detector massively. Thus, the interactions can be precisely monitored. Like COSINUS, the detector used in CRESST emits light as well after each interaction. The light emitted can be used to identify the particle responsible for the detected energy. [26]

3.3. Electron scattering and ionisation

Light Dark Matter detection cannot exploit the recoil of the nuclei due to dark matter interaction, since their mass is too small, to detect the energy transfer. Instead, interaction with smaller particles are required, namely electrons.

To cause ionisation, dark matter particles heavier than $1\,\mathrm{MeV}/c^2$ are needed. When using a semiconductor like silicon instead, the detection sensitivity can be increased significantly [27].

The kinematic of scattering of dark matter with electrons is more complex, than the one of nucleus - dark matter interactions. One reasons for this is, that electrons are not at rest, but typical have higher speeds then dark matter particles. Furthermore, electrons are not independent particles, instead they are bound. The structure of the electrons itself is complex in semiconductors, that are used for experiments. Due to energy conservation, the energy E_e transfer to the electron, is the energy lost by dark matter called ΔE_χ and the recoil energy of the whole atom E_N [21]:

$$E_e = -\Delta E_\chi - E_N \tag{3}$$

The energy of the electron E_e is not only the kinetic energy received, but the energy to move the electron to the conduction band as well. The recoil energy of the atom E_N will be ignored in later calculations. It is very small compared to the energy transferred to the electron, since the mass of light dark matter is so small.

The average velocity of the electrons is $v_e \approx Z_{eff}\ \alpha$, with the fine structure constant $\alpha \approx 1/137$ and the effective charge Z_{eff}, which is one for outer electrons. This leads to $v_e/c \approx 10^{-3}$, which is a high speed compared to the incoming dark matter.

To calculate the recoiled rate R, the variables shown in Tab. 1 are used:

ρ_{chi} :	local dark matter density
m_χ :	mass of a dark matter particle
N_{cell} :	number of unit cells in the target crystal
$\overline{\sigma_e}$:	parameterization of the strength of the interaction

m_e :	mass of the electron
μ_{χ^e} :	reduced mass of the dark matter-electron system
q :	momentum transferred
E_e :	energy transferred to the electron
$\eta\left(v_{min}(q, E_e)\right)$:	the dark matter velocity profile
$F_{DM}(q)$:	dark matter form factor
$f_{crystal}(q, E_e)$:	crystal form factor
$v_{min}(q, E_e)$:	minimum speed of dark matter particle needed to for electron to gain energy E_e

Tab. 1: The variables used to calculate the recoil rate R

The recoil rate can thus be calculated by [27]:

$$\begin{aligned}\frac{\mathrm{d}R}{\mathrm{d}\ln E_e} &= \frac{\rho_\chi}{m_\chi} N_{cell}\, \overline{\sigma_e}\, \alpha\, \frac{m_e^2}{\mu_{\chi^e}^2} \\ &\times \int \mathrm{d}\ln q\, \left(\frac{E_e}{q}\, \eta\left(v_{min}(q, E_e)\right)\right) \\ &\times F_{DM}(q)^2\, |f_{crystal}(q, E_e)|^2\end{aligned} \tag{4}$$

The dark matter form factor $F_{DM}(q)$ is necessary to calculate the momentum dependency of the interaction. For a point like interaction, which will be assumed, $F_{DM}(q) = 1$ [21].

The expected rate is $29\,\mathrm{events/kg\,day}$ for silicon with $m_\chi = 100\,\mathrm{MeV}/c^2$ [27]. During the scattering, on average Q electrons are produced. This number can be calculated, with the ionisation energy $E_{ion} = 3.6\,\mathrm{eV}$ and the gap energy $E_{gap} = 1.11\,\mathrm{eV}$. For dark matter particles with mass $10\,\mathrm{MeV}/c^2$, about 65% of all events generate at least two electrons in the detector, which is necessary to distinguish the event from thermal generated background single electron events:

$$Q(E_e) = 1 + \left\lfloor \frac{E_3 2e - E_{gap}}{E_{ion}} \right\rfloor \tag{5}$$

Here, $\lfloor\ \rfloor$ denotes the floor, meaning, the value in between is rounded down to the nearest integer [27].

4. Detection Methods

4.1. Semiconductors

Semiconductors have a valence band and a conduction band, separated by a band gap. The electrons need to be exited from the valence band to the conduction band, to be able to move inside the material and conduct a current. This happens when energy is deposited through temperature or radiation [28].

The semiconductor of choice is silicon, because it is well understood and therefor it is possible to accurately fabricate silicon semiconductors devices. Silicon is already used in many applications such as photovoltaic or microchips. In the following only silicon semiconductors will be covered.

Doping of semiconductors

Doping is the practise of putting small amounts of known impurities in the semiconductor to change its properties. Silicon is a group IV element in the periodic table. The semiconductor can be positively doped, or p-doped, with group III elements like boron. When using group V elements like phosphor the semiconductor can be negatively doped, or n-doped. [28]

Doping puts extra electrons and electron holes in the lattice of the semiconductor, which can move freely. If p-doped and n-doped semiconductors are connected to each other, there is a p-n junction. The holes and electrons recombine, creating a depletion zone with an electric field present (Fig. 6) [28].

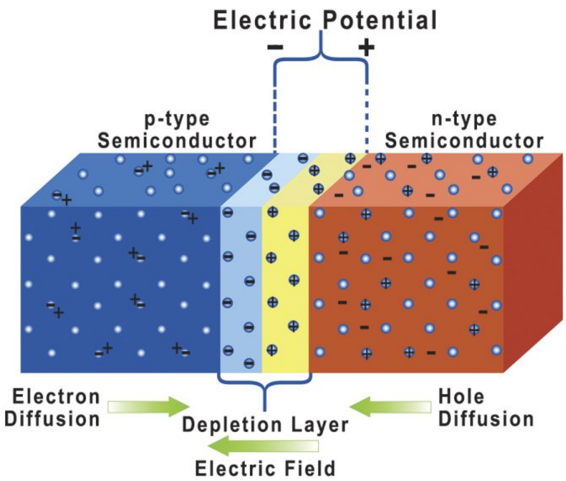

Fig. 6: An unbiased pn-junction is depicted. The depletion zone, as well as the charge carriers are visible. From [29].

Depending on the concentration of the doping agents in the silicon, the depletion zone reaches farther into the p- or n- doped part. The size of the depletion zone can be manipulated and controlled by applying a voltage across the junction. Without any additional reveres voltage, the junction is called unbiased, with a voltage present, it is called biased [28].

If a positive voltage is applied to the p-doped part, the junction is forward biased, and the depletion zone shrinks. If the positive voltage is applied to the n-doped part, the junction is called reversed biased, and the size of the depletion zone increases. If the voltage is large enough, the depletion zone extends over the whole semiconductor. In such a case, the silicon is called fully depleted [28].

Sideward depletion

Sidewards depleted structures are commonly used as radiation sensors. When radiation hits the silicon, electron - hole pairs are created. Within the depletion zone, the pair is separated by the electric field, making this the sensitive volume. Detectors made of fully depleted silicon provide the maximal sensitive volume and quantum efficiency due to the missing dead layers, and decreased capacitance. However, the total noise due to dark current – generated by thermal excitation per unit volume – increases [28].

For sideward depletion, two wavers with p-n junction are put together (Fig. 7), with the n-junctions connected. To both wavers, the same reverse bias is applied. This way, a large, depleted area arises between two p-junctions. The strongly doped n-junctions in the middle only serve as a contact, and can be moved relatively freely, to create a large sensitive volume [30].

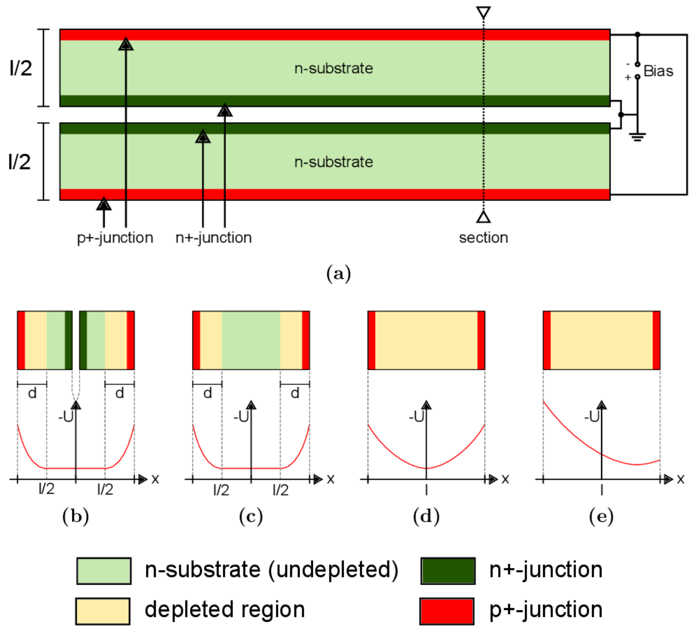

Fig. 7: For sidewards depletion, the waver can be seen as split in two sub-wavers, each with its own p- and n-junction. a) shows the connected wavers without a bias. In b) a bias is applied. The n-junction is not important for the mechanics and is ignored in c). It serves only as a contact and can be put on the outside. In d) the bulk is fully depleted, and the non-depleted conducting channel is suppressed. As shown in e), by using an unsymmetrical bias, the minimum can be shifted. Graphic from [28], modified from [30].

The thickness d of the depletion region can be calculated with the Voltage U, the dielectric constant ϵ, the electron charge e and the concentration of donors N_D [30]:

$$d = \sqrt{\frac{2\epsilon U}{qN_D}} \qquad d \leq l/2 \tag{6}$$

Without a bias voltage, there are two depletion zones between the n-junctions in the middle, and the p-junctions at the side (Fig. 7, b). The Potential does not change, if the strongly n-doped region is cut (Fig. 7, c). By applying a bias voltage, the whole waver can be depleted (Fig. 7, d). By applying an asymmetric bias voltage, the minimum can be shifted (Fig. 7, e).

For each of the sub wavers, Eq. (6) holds, each having half the thickens of the total waver. This shows that the setup has the benefit of needing only a quarter of the current as a traditional setup to completely deplete the waver. This has the benefit, that less leakage current is generated, therefor the measurements can be less noisy. When used as a detector, the electrons move towards the anode, while the holes move towards the p-implants [28].

4.2. Detection

Events are detected, by measuring the free electrons created by those events. Ideally, the received signal is proportional to the strength of the events.

General characteristics

Depending on the setup, a transport field is needed to direct the electrons to the readout node with more direction than just through diffusion. The size of the anode is proportional to its capacitance and noise. The capacitance can be reduced by reducing the size of the anode. With the right transport field present, the anode can be reduced to a point for smallest capacitance, and therefor least noise. This means the detector size can be increased, without increasing the capacitance.

Silicon drift detectors

To the fully depleted detectors, an electric field parallel to the surface is applied. This creates an additional lateral drift field, which drives the electron to the collection anode, increasing the speeds of the process [31]. To do this, the p-implantations are segmented and connected to a voltage cascade, as seen in Fig. 8 [28]. Such detectors are called *silicon drift detectors* (SDDs).

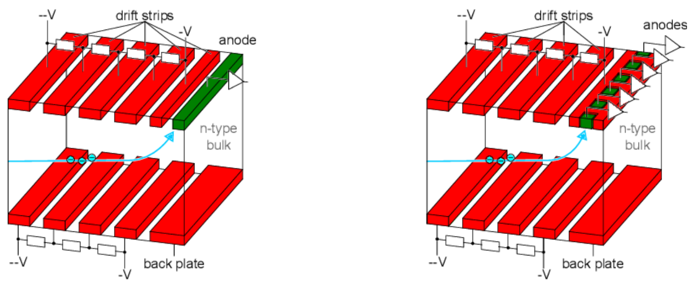

(a) linear SDD (b) matrix SDD

Fig. 8: Different SDDs are shown. a) In a linear SDD only one-dimensional position resolution is possible by using the drift time of the electrons. b) In a matrix SDD two-dimensional position resolution can be achieved by using drift time for one dimension, and the anode which detected the signal for the second dimension. From [28].

When using a circular detector instead (Fig. 9), the anode capacitance is comparatively small. This is because the capacitance is independent of the detector area. The circular SDDs have good energy resolutions and peak-to-background ratios [31].

Stray capacitances of the connections are suppressed by the *field effect transistor* (FET) in the center of the detector's p-field rings. This configuration makes the matching between the detector and the electronics easier than is possible with a non-circular SDD [31].

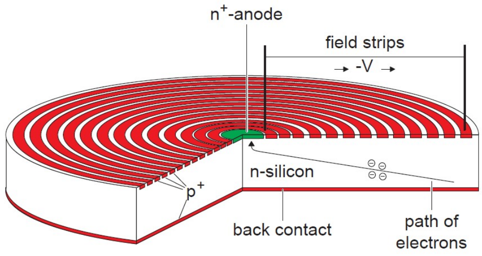

Fig. 9: The circular SDD has a front contact, that is segmented into p-implant rings. The applied voltage cascade overlays the depletion field with a lateral drift field, guiding the electrons to the center of the detector [28].

CCD detectors

The next step in sideways depleted detectors is p-n *charge-coupled device*s (CCDs). Although similar in composition as the SDD in Fig. 8, in a p-n CCD, the individual strongly p-doped strips are not connected to form a voltage cascade. Instead, every third strip is connected to a common voltage node, forming a shift register (Fig. 10) [28].

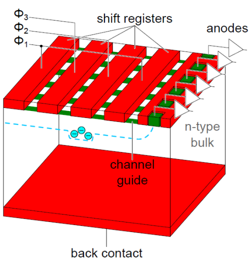

Fig. 10: The CCDs are sidewards depleted. The shift registers have the voltages Φ_1, Φ_1 and Φ_3. Thus, pixels are formed, where the electrons created in the bulk are collected. To read out the CCD, a voltage sequence is performed, and the charges are transported to the readout node. From [28]

To avoid a spreading of the charge cloud, channel guides are formed by n-doped stripes in the surface region. The potentials of the shift registers and the guide channel's divide the detector into pixels. Electrons, that are excited to the conduction band drift to the potential minimum, and remain there, until they are read out. The readout is done by periodical shifting the voltage of the shift registers, thereby moving the electrons to the readout node. The position is then proportional to the number of shifts needed to get the electron.

Just like the circular SDD, the backside of the pn CCD is a homogeneous large area, giving them a large quantum efficiency. The CCDs also have a FET integrated at the readout node for a first amplification.

4.3. DePFET detectors

The *depleted p-channel field effect transistor* (DePFET) is a sideways depleted detectors with an integrated collection and storage node, combined with a first stage of amplification (Fig. 11). Different than the CCD, which transports the charges form the pixels to the readout node, a DePFET has a readout node at each pixel, called an active pixel [28].

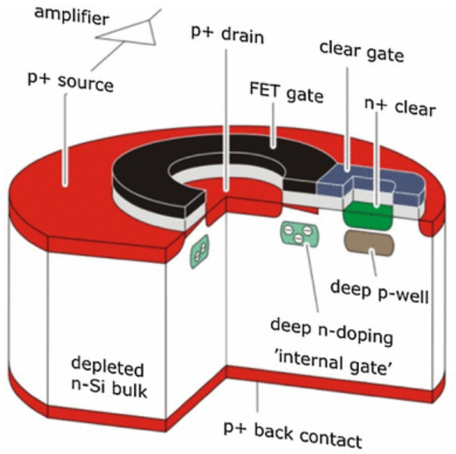

(a) The DePFET cell

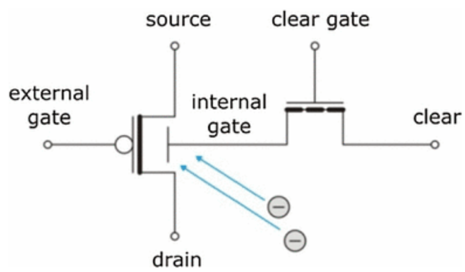

(b) Circuit of a DePFET

Fig. 11: DePFET schematic and circuit. The deep p-well below the clear protects the DePFET from charge losses, when they are not desired [21].

Electron-hole pairs that are created in the depleted bulk drift to the deep n-implant below the gate, which is a minimum. There, they influence the mirror charges, which changes the conductivity of the transistor channel the same way as electrons in the transistor gate would do. This potential minimum is therefore referred to as the internal gate [21].

This means, the DePFET has basically a *metal-oxide semiconductor field effect transistor* (MOSFET) attached to the bulk, as seen in the schematic of Fig. 11b.

To remove the charges after a measurement, a clear contact is integrated. This is a strongly n-doped part of the DePFET. To prevent charge losses, below the clear contact is a deep p-well to shield the clear. The clear is surrounded by the clear gate, a MOSFET structure. The clear gate forms a connection between the clear contact and the internal gate. By applying a positive pulse to this structure, the charge in the DePFET can be removed.

The source is the source of charge carriers, forming the current for the DePFET, while the drain is the current sink. The current only needs to be present during the read out of the detector and can be turned off at signal integration. Thus the DePFET combines the properties of a sensor, an amplifier and signal charge storage. They have fast gathering, analog storage, and RNDR readout without reset noise [32].

To get a high accuracy measurement from a DePFET detector, the channels conductance is sampled, then the charge from the internal gate is removed via the clear contact, then the conductance is sampled again. This is *correlated double-sampling* (CDS), and is done by first measuring the baseline plus the collected charge, and then remove the baseline from it with the second measurement. DePFETs can thus be operated with an *equivalent noise charge* (ENC) of less than $3e^-$ *root mean square* (RMS) with a readout time of $3.5\,\mu s$. [33]

The DePFET is a p-channel FET, so a negative voltage is required to switch on the detector. For the clear process, a positive voltage is applied to the clear contact, then the clear gate is opened, to remove charges. After closing the gate again, the clear contact is switched to a more negative voltage, to prevent charge loss.

4.4. RNDR DePFET detectors

By using *repetitive non-destructive readout* (RNDR), the noise can be reduced by regression to the mean. The charges collected in the internal gates have a long lifetime, losses can thus be neglected. DePFETs are especially suited for RNDR measurements, with the pixel-individual charge storage and readout at high speed with very good SNR detectors [21].

The charges are measured repeatedly and statistically independent n times, thus the average measurement has a standard deviation of $\sigma_{eff} = \frac{\sigma}{\sqrt{n}}$, with σ as the RMS of a single measurement, for more information about this, see section 5.3.

Since the charge is measured indirectly through the channel conductivity, a DePFETs can instead of clearing the charges away after the measurement, store them in an adjacent storage node. There, the charges have no impact on the channels conductivity, thus mimicking the clear process and implementing a non-destructive CDS. The charge can be loaded back in the DePFET to start a new cycle of CDS [21].

The storage node can be the internal gate of a second adjacent DePFET with a transfer gate between them. The charge can thus be measured arbitrarily often by each DePFET, before the charge is cleared with the clear gate. Those pixels can be described as super-pixels, with each DePFET being its own subpixel (Fig. 12) [21].

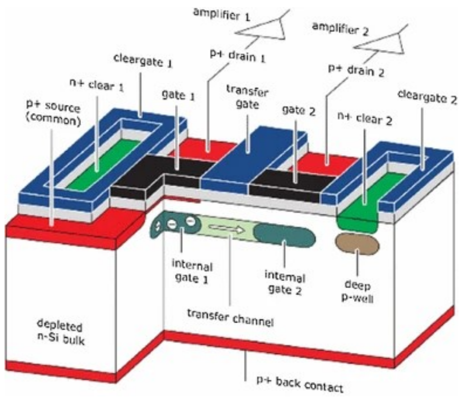

(a) A cut through a RNDR DePFET super-pixel.

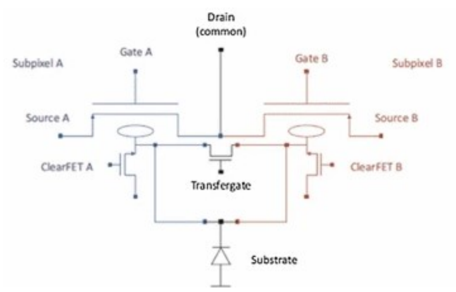

(b) Circuit of a RNDR DePFET.

Fig. 12: The RNDR DePFET super pixel, made of two sub pixels. The subpixels transfer the charge via their transfer gates as often as desired. From [21]

5. Noise

The terminus noises summarizes random or unwanted signals, that disturb the measurements. To be able to get precise measurements, it is important to control and suppress noise. There are different kinds and sources of noise, discussed below.

5.1. General kinds of noise

Thermal- or white noise

White noise is a random signal with about equal intensity over the whole frequency spectrum. Analogue to visible light, this would result in a white colour, hence the name. Thermal noise is generated due to the thermal movement of the charge carriers. In the DePFET, the resistance of the transistor channels is affected by thermal noise. The modulation of the current at the channel I_{DS} is the noise voltage source at the gate [34]:

$$\frac{\mathrm{d}\overline{U_n^2}}{\mathrm{d}f} = 4k_BTR \tag{7}$$

with the absolute temperature T, the resistance R and the Boltzmann constant k_B. For field effect transistors, the resistance concerns the channel, and it can be calculated by $\Gamma\frac{1}{g_m}$, with the transistor conductance g_m of the transistor and the manufacturing process dependent factor Γ, with $\Gamma = 2/3$ for Metal-Oxide-Semiconductors.

1/f- or pink noise

Pink noise or 1/f noise dominates at low frequencies. In the visible light spectrum, such a noise would appear as a pink colour, hence the name. The first approximation of this noise is the reciprocal of the frequency f. In a FETs, this noise is generated by temporarily trapped charges in the transistor channel. They create mirror charges, which change the conductivity of the channel. In FETs, most traps lie at the boundary between the bulk, and the oxide. It is therefore beneficial for the channel to be located in the bulk at a distance from the surface [34].

$$\frac{\mathrm{d}\overline{U_n^2}}{\mathrm{d}f} = \frac{A_n}{f^\alpha} \qquad \alpha \approx 1 \tag{8}$$

In this equation, f is the frequency, and A_n is a device specific constant.

Shot noise or Poisson noise

Shot noise can be modelled by a Poisson distribution. It is due to the quantisation of charges and can only happen, if there is a current present in the device. When a current I circulates, then during the time Δt a charge of $\Delta Q = \Delta N \cdot e$ crosses a boundary. The current I is only the average amount of charge carriers passing during a time. The actual amount of passing current is random. The statistical fluctuations are $\delta\Delta N = \sqrt{\Delta N}$, which correspond to the mean current $\langle\delta I^2\rangle = \frac{Ie}{\Delta t}$. The frequency power spectrum for a reversed bias detector, like a DePFET, is [34]:

$$\frac{\mathrm{d}\overline{I^2}}{\mathrm{d}f} = 2I_L\,q \tag{9}$$

with the leakage current I_L and the charge q.

5.2. Dark current

Dark current or leak current is generated due to the depletion voltage. It is generated when electrons and holes are generated randomly mainly due to thermal energy, without being stimulated by events. It is composed of a fixed pattern noise, which can be filtered with repeated measurements. However, there is a random shot noise in the dark current as well, which cannot be directly filtered. Dark current can be suppressed by decreasing the temperature to cryogenic values. The measurements are taken at $(60 - 150)\,\mathrm{K}$.

5.3. Noise in DePFET detectors

Depleted p- Channel Field Effect Transistor (DePFET) detectors have very low noise, leading to a good SNR even at very small signals. To explain how this is archived, first the noise for a single readout will be discussed before focusing on repetitive readouts and the noise associated with it.

Single readout noise

The *equivalent noise charge* (ENC) of a single readout is the sum of white noise from thermal fluctuations of the charge carriers in the transistor channel n_w, white noise from the leak current in the detector volume w_l and the 1/f, called n_f. The 1/f noise is due to the capture and re-emission of charges in the transistor channel. The charges are trapped in defects. Each defect has a different trapping time, with longer trapping times over-represented, which results in the 1/f noise [32].

The leak current can be suppressed sufficiently by cooling the detector. While its contributing is shown in the formula for the total ENC, the noise resulting from W_l will be ignored in the further analysis [32]:

$$ENC^2 = \frac{w_c}{\tau} C_{tot}^2\, A_1 + 2\pi\, n_f\, C_{tot}^2 A_2 + w_l\, \tau\, A_3 \tag{10}$$

In this formula, C_{tot} is the capacitance of the system, A_1, A_2 and A_3 are filter parameters with a weighting function and τ is the shaping time mapped to the time needed for a measurement.

As seen in Eq. (10), the shaping time τ does not affect the 1/f noise. However, for white noise, this is not the case. The noise is inversely proportional to the shaping time τ.

The shaping time can be increased to decrease the noise. The time can be taken arbitrarily large. With longer shaping times τ, the noise decreases, up to the point, when the 1/f noise dominates. In Fig. 13, a triangular weighting function is chosen. The different readout times only affect the white noise [32].

Noise during RNDR

With the total measuring time τ_{tot} fixed at a value where the 1/f noise dominates, the ENC does not change by much for $\tau > \tau_{tot}$. Since the ENC is calculated by setting the *noise-to-signal ratio* (N/S) to one [32]:

$$\left(\frac{N}{S}\right)^2_{white,single} \propto A_1 \frac{1}{\tau_{tot}} \tag{11}$$

$$\left(\frac{N}{S}\right)^2_{1/f,single} \propto A_2 \tag{12}$$

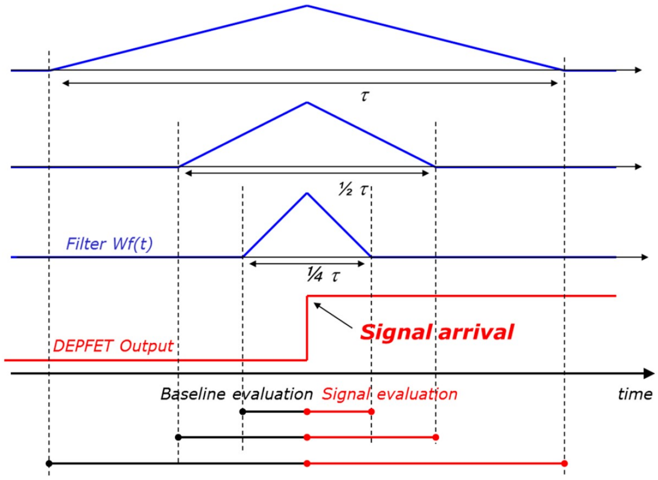

Fig. 13: The red line is the signal received from the DePFET. This same signal is processed with three different shaping times τ. From [34]

Using *repetitive non-destructive readout* (RNDR), the charges in the DePFET are moved back and forth n times. Thus, the signal is measured n times to build the average of these values. Since τ_{tot} is fixed, each measurement takes the time τ_{tot}/n.

The RMS of each individual measurement is lager, then by just taking one long one. But this is compensated by averaging over the n measurements. Therefore, for white noise, there is no improvement resulting from this method [32]:

$$\left(\frac{N}{S}\right)^2_{white,many} \propto \frac{n\left(A_1\frac{n}{\tau_{tot}}\right)}{n^2} = A_1\frac{1}{\tau_{tot}} \tag{13}$$

However, the 1/f noise is independent from the shaping time τ. Therefore, the noise of the individual measurements stays the same. Since the individual measurements are independent of each other, the noise decreases leading to a N/S [32] :

$$\left(\frac{N}{S}\right)^2_{1/f,many} \propto \frac{nA_2}{n^2} = \frac{A_2}{n} \tag{14}$$

In other words, while the white noise stays fixed with the number of measurements per time τ_{tot}, the 1/f noise decreases with $\sqrt{n}$, if the noise for each measurement is totally uncorrelated. Otherwise, it decreases with $\sqrt{n^\alpha}$ with α close to one. The weighting function $\mathrm{Wf}(t)$ for RNDR, with the Heaviside function $\mathcal{H}$ is [32]:

$$\begin{aligned}\mathrm{Wf}(t) = \frac{1}{\tau}\sum_{k=1}^{n}\Bigg\{&\left(t-2\frac{\tau\,(k-1)}{n}\right)\cdot\mathcal{H}\left(t-2\frac{\tau\,(k-1)}{n}\right)\\ &-2\left(t-2\frac{\tau\,(2k-1)}{n}\right)\cdot\mathcal{H}\left(t-2\frac{\tau\,(2k-1)}{n}\right)\\ &+\left(t-2\frac{\tau k}{n}\right)\cdot\mathcal{H}\left(t-2\frac{\tau k}{n}\right)\Bigg\}\end{aligned} \tag{15}$$

Here, the shaping time τ is the complete readout time of all n measurements. The coefficients A_1 and A_2 are calculated as follows [32]:

$$A_1 = \int_{-\infty}^{\infty} [\mathrm{Wf}'(y)]^2 \mathrm{d}y \tag{16}$$

$$A_2 = \int_{-\infty}^{\infty} [\mathrm{Wf}^{\frac{\prime}{2}}(t)]^2 \mathrm{d}t \tag{17}$$

$$\tag{18}$$

Here, $y = t/\tau$ is the time normalized to the shaping time, and A_2 is calculated using the half derivative. Calculating this, $A_1 = 4$.

According to [32], the values are $A_1 = 4$ and for A_2, the values are given in Tab. 2:

Number of Readouts n	A_2
1	0.88254
2	0.38287
4	0.17038
8	0.07823
16	0.03695
32	0.01782

Tab. 2: The values for A_2 for different numbers of repetitions n. From [32]

The filter parameter, and therefore the white noise component of the ENC is reduced to about 2% for 16 repetitions, compared with the same measurement with no repetition. Increasing the number of readouts therefore decreases the noise significantly.

Part II: The experimental setup

6. The setup of the DANAE experiment

The *direct dark matter search using DePFET with repetetive non-destructive readout application experiment* (DANAE) is an experiment for direct searches of light DM through DM - electron interactions. The experiment is located at the *Institut für Hochenergiephysik* (institude of high energy physics, HEPHY), an instiute of the ÖAW. It is motivated by the lack of evidence for WIMPs by experiments searching for them by using the interaction between dark matter and nuclei.

6.1. General setup of DANAE

Since the DePFET detector is very sensitive with respect to radioactive radiation, sources of those must be eliminated. As a first step, the detector is placed in a vacuum chamber. This chamber is evacuated to a pressure of about 5×10^{-6} mbar (0.5 mPa). This prevents that radioactive nuclei such as C^{14}, that exist in the air, cause background radiation due to decays, which interacts with the detector.

In future setups, the detector will be shielded with lead as well, and at the inside of the vacuum chamber only copper will be used, in order to not bring any impurities into the experiment. This has not been realised for the surface runs, recorder up to now.

The senor is mounted on a ceramic, which is connected to a relatively large thermal mass, that is cooled by a cold finger connected to a Stirling-cycle cryostat. The sensor is in thermal equilibrium through a thermal contact and radiation exchange with the this mass. An outer shielding block is located around the inner block, which is in equilibrium with the cooled inner mass (Fig. 14a). This decreases the lowest possible temperature of the inner mass, because then there is another cascade between the cold finger and the environment.

Holes are added on the upper side of the shielding blocks. Those are aligned directly above the sensor, in order to enable its exposure to radiation sources, if needed for calibration purpose. For instance, a LED is fixed on a movable plate, and a radioactive iron probe can be fixed there as well. Using those, the response of the detector was studied.

The crycostat is capable to reach temperatures as low as 60 K (-213.15 °C), which is necessary to reduce dark current, which induces noise in the measurements. Temperature sensors are mounted on the thermal masses to monitor the temperature of the detector. The whole setup is shown in Fig. 14b.

The different voltages and currents are supplied by ten DC power supply devices with three channels each and a single one channel high voltage power supply. The 31 different voltages can be operated remotely. They are connected to the detector with a cable harness. The operation of the detector is monitored via a connected oscilloscope. This gives feedback to the functionality of the setup.

The sensor is connected to the *readout board* (ROB) via a 70 mm double layered flex-PCB. The ROB is placed in the vacuum chamber, due to the fact, that the length of the flex-PCB as to be limited because of the high frequency that is used for the condole and readout of the detector would otherwise induce to much noise.

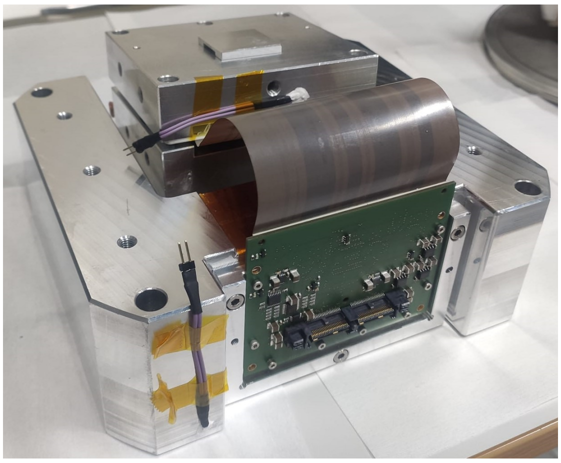

(a) The temperature shielding of the detector. The detector is below the hole in the inner shielding. The top part of the outer shielding was removed for the inner part to be visible. The readout board is fixed to the outer shielding.

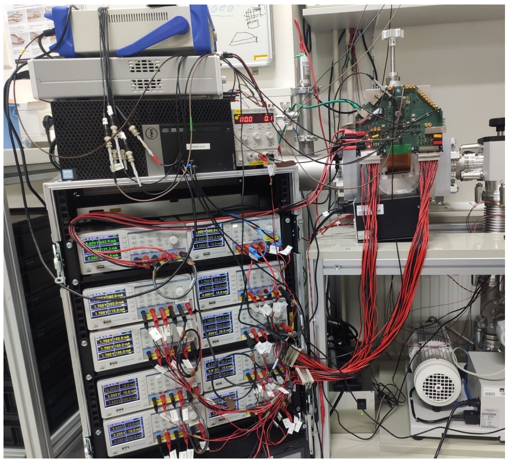

(b) The whole setup, including the power sources on the left. In the bottom right, the vacuum pump is visible. The cryostat is behind the vacuum chamber.

Fig. 14: The setup of DANAE. In future setups, additional lead shielding will be implemented, and the aluminium temperature shielding will be replaced with copper.

Using another flex-PCB, the ROB is connected to the *multi-functional board* (EPP) outside the vacuum chamber. This board is connected to the power supplies for the different voltages needed. The EPP hosts a Mercury *field programmable gate array* (FPGA) chip for control.

Contacts on the EPP are used to connect an oscilloscope for immediate feedback on the functionality of the setup. Other connections can be used to check the proper working of singular components, like the SwitcherS. The EPP interfaces with the external commercial power supply modules, then regulates and distributes the voltage or current sources to the *application specific integrated circuit*s (ASICs) on the ROB. It hosts a Mercury KX1 FPGA, with which the sequence of the power supplies to the ASICs is defined and thus determines the RNDR operation of the DePFET matrix. The FPGA also defines the sequence of acquiring the output from the front-end amplifier and communicating via the interface to the *personal computer* (PC) for digitization and acquisition. Further details are explained below. The EPP provide the debugging and monitoring platform during the implementation of the control and readout sequence.

6.2. The readout board

The board controls the DePFETs, when the charge is transferred, cleared and read out. This is done using one Veritas 2.1 chip, and two SwitcherS chips. The Veritas samples the columns for readout, while the Switcher East and West control the rows. The Switcher North is not needed or connected for DANAE. While it is present in Fig. 15, it is included in the setup to enable a modular adaption for future changes or differnet projects.

The two most important components of the front end electronic are discussed in the following paragraphs. The SwitcherS and the Veritas (Fig. 16).

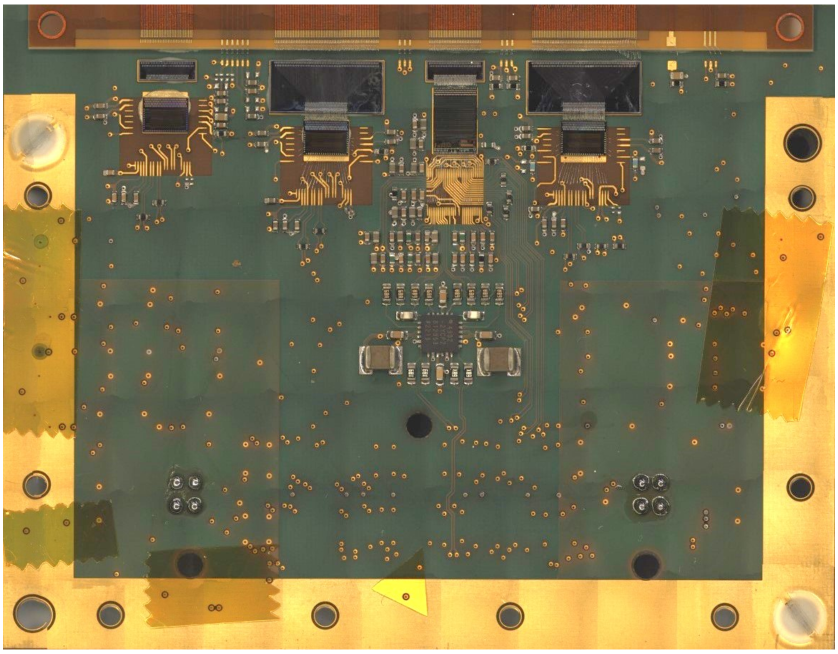

Fig. 15: The ROB of the DANAE-detector. The Veritas and Switcher are visible at the top.

SwitcherS

The SwitcherS (Fig. 16a), is an analog multiplexer ASIC to control the rows of the DePFET detector. It was developed by Steinbeis-Transferzentrum Microelectronics and Sensor System and has 64×2 channels, or 64 channels with a switch in each of them. The SwitcherS uses a shift register to select the channels. To enable a channel, two load signals are necessary. This way, the chip needs less power in idle mode [35].

The shift register to change channels as well as the missing of an internal configuration register makes the SwitcherS very stable. To still be able to monitor possible SEU problems, the chip as a heartbeat signal [35]. The two SwitcherS are used to control gate 1 and gate 2, as well as clear, clear gate and the transfer gates.

Veritas

The *versatile readout based on integrated trapezoidal analog shapers* (Veritas) (Fig. 16b), is a 64-channel front-end readout ASIC developed by Max-Planck-Institut for Extraterrestrial Physics and is used to read out the DePFET detector. It has a clock speed of $20\,\mathrm{ns}$, it can read out one row of the detector in $(2-3)\,\mu\mathrm{s/row}$. It uses a *serial peripheral interface* (SPI) for control. The ENC for a DePFET detector is less than 5 electrons RMS with an integration or signal shaping time of $t_{int} = 1\,\mu$s. [36]

The Veritas is used in *drain current readout* (DR) mode for DANAE. In this mode, the nodes of the DePFET all have a fixed potential, and the inertia of the system is not limited by the RC time constant [36]. A schematic of the operation of the Veritas is shown in Fig. 17.

The DePFET bias is large compared to the signal current. Because of dispersion in the matrix, the correction must be done pixel wise, a fixed current source is used for this [36]. With an active cascade, the detector input is decoupled from the amplification stage. Afterwards, the current signal form the detector is translated to a voltage. Subsequently the signal is sent to the pre-amplifier [36]. The Veritas as two *static random access mem-*

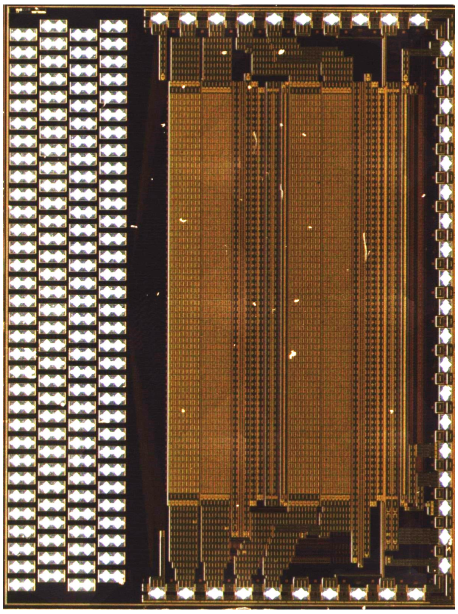

(a) The SwitcherS is displayed. The contacts on the left connect to the detector. The size of the SwitcherS is $(3575 \times 4750)\,\mu\mathrm{m}^2$.

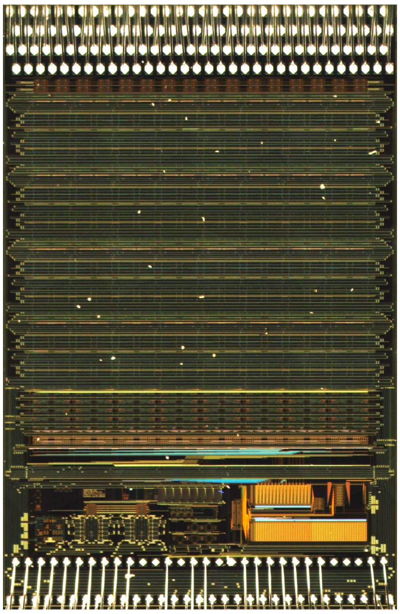

(b) The Veritas is displayed. The contacts on the top connected to the detector. The size of the Veritas is $(4593 \times 7046)\,\mu\mathrm{m}^2$.

Fig. 16: The Switcher and the Veritas are shown here. On the ROB there is one Veritas and two SwitcherS.

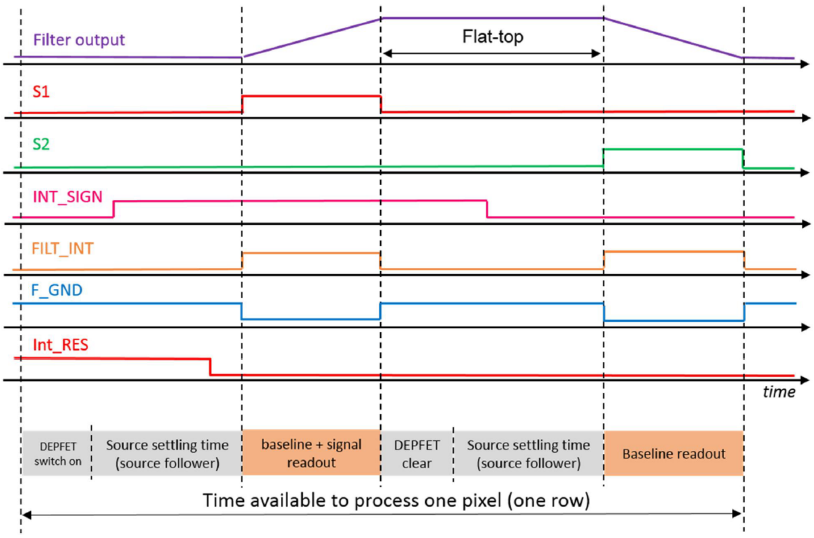

Fig. 17: The source follower readout mode of the Veritas. For the drain current readout mode, the Source settling time in the diagram is near to zero. From [36]

ory (SRAM) fields, one is the Sequencer *random access memory* (RAM), which operates the timing control and filter stage. The configuration RAM is responsible for the static settings of the ASIC [36].

6.3. Characteristics of the detector

The detector, which is shown in Fig. 18 is made up of a 64×64 matrix of RNDR DePFET pixels. In other words, there are 4096 active pixels, each pixel consisting of a DePFETs super pixels for repetitive non-destructive readout.

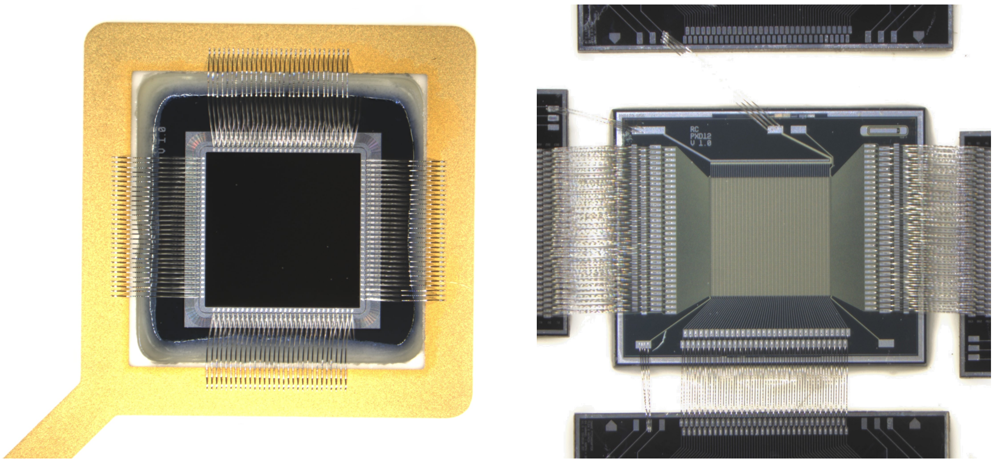

(a) The DePFET cell from the top. **(b)** The DePFET cell from the readout side.

Fig. 18: The DePFET-detector from both sides. The connections to the readout board are visible.

The sensor has an area of $3.2\,\mathrm{mm} \times 3.2\,\mathrm{mm}$, with a depth of $450\,\mu\mathrm{m}$. The sensitive volume of the detector used in DANAE is $24\,\mathrm{mg}$ of silicon [37]. This volume is only reached, if the detector is fully depleted. For this, a back voltage of $110\,\mathrm{V}$ is supplied, with the connection (Fig. 18a).

The DePFET pixels of the sensor are controlled and read out through the connected wire bonds (Fig. 18b). The different connections are named after the side they are from. The sensor is located in a coordinate system in a way, that the top is called north, the right side corresponds to east, the left side is called west and the bottom side is the south side. The SwitcherS are connected to the east and west side, while the Veritas is connected at the south side.

6.4. Supply Voltages

As shown in Fig. 14b, the DANAE has several power supplies for different functions in the setup. The different supply voltages, the current limits and the actual currents of the new and old detector are shown in Tab. 3.

Supply Voltage	Voltage (V)	Current Limit (mA)	Current new (mA)	Current old (mA)
5 Volt	5	1000	627.3	634.1
+5V	5	900	124.0	103.6
-5V	5	1000	136.3	125.4
VDD	1.7	380	293.6	215.3
VSS	1.7	350	231.9	216
VDD_AC	1.7	110	49.3	20.5
VDD Buffer	1.7	100	11.9	13
VSS Buffer	1.7	100	11.7	12.7

VSS_AC	1.7	100	43.7	20
Clear High	16	20	9.1	6.2
Clear Low	3.2	10	0	0
Transfergate High	8 / 7	20	0.1	0.2
Clear Gate High	9	20	9.1	6.2
Clear Gate Low	2.1	10	0	0
Transfergate Low	3.5	20	0	0
MOS	0	500	2.4	0
CHSep	10	500	2.4	1.1
Inner Sub	9	10	0	0
DVDD	1.7	50	3	2.9
DVSS	1.7	50	13.5	13.4
VSSS	0 / 3.5	120	0	6.2
VDD I2V	1.7	250	85.8	49.5
VSS I2V	1.7	250	153.2	48.9
Source Drain	0 / 3.5	120	0	6.2
Gate High	8.25	30	18.4	15.4
Gate 1 Low	0.898	20	5.2	5
VSWC_VDD	3.3	90	75.4	10
V_LED	0	25	0	0
Gate 2 Low	0.78	10	4.8	4.7
VSWC_SUB	7	75	25.6	16.3
V_Back	110	0	0	0

Tab. 3: The voltages and currents for the different supply voltages. For the channels, the voltages where different for the old and the new detector.

In order to be able to exchange the detector module, or to chain multiple detectors together, they have to show similar behaviour for the same supply voltages. Whether the behaviour is similar can be determined by the current drawn for the two detectors tested.

The differences between most of the currents is negligible, for other supply voltages however, there are quite big discrepancies. The new detector includes a faulty SwitcherS, which might explain the differences. If this is still the case with fixed components, then the voltages have to be adjusted for different detectors. In this case, chaining sensors together is not quite as straight forward as just connecting them. Instead, the voltages would need to be adjusted between the sensors, which would make the whole process more complicated.

7. Operation of the Detector

For the operation of the detector, a sequence is generated. This is done with an Excel document with embedded macros. Those macros translate the output to a proper format, that can be read by the FPGA. It is segmented in three parts, the instruction sheet, the pattern sheet and the output.

In the instruction sheet, the sequence is defined, how many repetitions are used, and the hold time. References to the pattern sheet are made there, which are the actual orders sent to the SwitcherS and the Veritas. The output sheet is generated automatically from the instructions and the pattern. Two *.tex* files are generated as well with the same output.

7.1. The pattern sheet

The pattern sheet has 32 different columns. They represent different Veritas inputs and SwitcherS inputs, generated by the FPGA. Each cell is binary, it can have either a value of 0 or 1. A part of the pattern sheet is shown in Fig. 19.

	ADC_AUX0	ADC_AUX1	ADC_CLK	Foramt0	Format1	MCLK	SCLK	SW_CLK	SW_Load	Second Gate	First Gate	SW_North_	Clear Gate
Pattern addr	0	1	2	3	4	5	6	7	8	9	10	11	12
0	1	1	1	0	0	0	0	0	1	0	1	0	0
1	1	1	1	0	0	0	0	0	1	0	1	0	0
2	1	1	1	0	0	0	0	1	1	0	1	0	0
3	1	1	1	0	0	0	0	0	1	0	1	0	0
4	1	1	1	0	0	0	0	0	0	0	1	0	0
5	1	1	1	0	0	0	0	0	1	0	1	0	0
6	1	1	1	0	0	0	0	0	0	0	1	0	0
7	1	1	1	0	0	0	0	1	0	0	1	0	0
8	1	1	1	0	0	0	0	0	0	0	1	0	0
9	1	1	1	0	0	0	0	0	1	0	1	0	0
10	1	1	1	0	0	0	0	0	0	0	1	0	0
11	1	1	1	0	0	0	0	0	0	0	1	0	0
12	1	1	1	0	0	0	0	0	0	0	1	0	0
13	1	1	1	0	0	0	0	0	0	0	1	0	0
14	1	1	1	0	0	0	0	0	0	0	1	0	0
15	1	1	1	0	0	0	0	0	0	0	1	0	0
16	1	1	1	0	0	0	0	0	0	0	1	0	0
17	1	1	1	0	0	0	0	0	0	0	1	0	0
18	1	1	1	0	0	0	0	0	0	0	1	0	0
19	1	1	1	0	0	0	0	0	0	0	1	0	0

		MPD1	MPD2	Clear	MPD_4	SWE_SIN_B	SWE_SIN_T	SWW_SIN_B	SWW_SIN_T	Frame Key	gen purpose	ADC Trig	Five/Key	GPIO?					
Pattern addr	13	14	15	16	17	18	19	20	21	22	23	24	25	26	27	28	29	30	31
0	0	0	0	0	0	0	0	0	0	0	0	0	0	0	0	0	0	0	1
1	0	0	0	0	0	0	0	0	0	0	0	0	0	0	0	0	0	0	1
2	0	0	0	0	0	0	0	0	0	0	0	0	0	0	0	0	0	0	1
3	0	0	0	0	0	0	0	0	0	0	0	0	0	0	0	0	0	0	1
4	0	0	0	0	0	0	0	0	0	0	0	0	0	0	0	0	0	0	1
5	0	0	0	0	0	0	0	0	0	0	0	0	0	0	0	0	0	0	1
6	0	0	0	0	0	0	0	0	0	0	0	0	0	0	0	0	0	0	1
7	0	0	0	0	0	0	0	0	0	0	0	0	0	0	0	0	0	0	1
8	0	0	0	0	0	0	0	0	0	0	0	0	0	0	0	0	0	0	1
9	0	0	0	0	0	0	0	0	0	0	0	0	0	0	0	0	0	0	1
10	0	0	0	0	0	0	0	0	0	0	0	0	0	0	0	0	0	0	1
11	0	0	0	0	0	0	0	0	0	0	0	0	0	0	0	0	0	0	1
12	0	0	0	0	0	0	0	0	0	0	0	0	0	0	0	0	0	0	1
13	0	0	0	0	0	0	0	0	0	0	0	0	0	0	0	0	0	0	1
14	0	0	0	0	0	0	0	0	0	0	0	0	0	0	0	0	0	0	1
15	0	0	0	0	0	0	0	0	0	0	0	0	0	0	0	0	0	0	1
16	0	0	0	0	0	0	0	0	0	0	0	0	0	0	0	0	0	0	1
17	0	0	0	0	0	0	0	0	0	0	0	0	0	0	0	0	0	0	1
18	0	0	0	0	0	0	0	0	0	0	0	0	0	0	0	0	0	0	1
19	0	0	0	0	0	0	0	0	0	1	0	0	0	0	0	0	0	0	1

Fig. 19: A part of the pattern sheet. In the top row, the names of the columns are displayed. The first column is the address for the instruction sheet.

Each row is numbered consecutively, to provide an address for the instruction sheet. While there are 32 columns, not all of them are used. Which row is executed is defined by the instruction sheet. Generally, the order of the rows is not important, unless a block of rows is executed consecutively.

The commands defined are the basic building blocks of the program executed by the detector. While the pattern sheet defines what commands are sent, the instruction sheet determines, when the commands are sent, and in which order.

7.2. The instruction sheet

The instruction sheet enables the user to change the operation of the detector. The instructions on the pattern sheet are more general. For changes in operation the instruction sheet is modified, not the pattern sheet. To program the detector, several operations are available.

Similar to the pattern sheet, every row has an address. There are four columns to provide instructions, then a 32-bit data sheet, followed by four columns of commands for the pattern sheet.

Each operation takes on clock to execute. The clock length can be varied but is set to $20\,\mathrm{ns}$ for the used configuration. When a part of the pattern is executed, the length it takes can be calculated, by multiplying the number of words executed by the number of cycles and the hold time. To each of the numbers one clock must be added, to get the right duration. An example is given in Fig. 20.

PATTERN COMMANDS			
Address	# words	# cycles	hold time
40	41	42	43
12 bit - DEC	12 bit - DEC	12 bit - DEC	12 bit - DEC
140	2	63	4

Fig. 20: An example from the instruction sheet, to see how to calculate the length of the command. This line takes 960 clocks.

The address at the pattern sheet is 140 (Fig. 20), and the number of words is 2. This means three lines from the pattern are executed, starting at line 140. They are repeated 64 times and hold for 5 clocks. For instance, this command takes 960 clocks, or 122.88 µs to execute.

A 12-bit architecture is used, therefore the highest number for the number of cycles and the hold times is 4095. The instruction sheet is generally executed line by line, except if there are jump commands present. In that case, an address for the destination of the jump is necessary. There are *conditional jumps* (JCRs) and *unconditional jumps* (JMPs). Further, commands like conditional loops are summerized in Tab. 4.

Command	Description
ACC	Adds or subtracts the data value from register value pointed too by operand
JCR	Conditional Jump
JMP	Unconditional Jump
LI	Load Immediately
NOP	No Operation

Tab. 4: Important commands and its descriptions.

The commands can have further register operations. Those specify the actual operation taken because of the command. The most important of those operation options are shown in Tab. 5.

Register Operand	Description
DCLK	A register used as a counter for the number of repetitions
FREE	Number of free words left in stack
PLL	Sets the PLL output clock period for the S7 with default of 50MHz
SADR	This register pushes the data to the Pattern RAM readout instructions stack

Tab. 5: Important register operations and its descriptions.

This tool enables the generation of complex programs. The exposure time, the number of cycles for the RNDR and the exact configuration of the charge carriers transfer to the clear are defined by the program. The frames are labeled for future analysis.

7.3. Output

After the program has been written, it is translated to a proper format, which is readable by the FPGA. For this, macros are embedded in the excel sheet. Two output files are generated, one for the pattern RAM, and one for the sequencer RAM. The same output is written to the third sheet of the excel file.

The files created, are plain text files, with *inter-integrated circuit* (I^2C) commands. I^2C is a serial data BUS system, where the data transfer in all directions is always initiated by the controller. With those, the whole setup is piloted. The commands are numbers in hexadecimal and are made up of the address of the device and the instruction. An example is shown in Fig. 21.

```
GPIO w 0x40018528 0x80000207
GPIO w 0x4001852C 0x80000207
GPIO w 0x40018530 0x80000207
```

Fig. 21: A part of the pattern RAM is shown. The individual lines are I^2C commands.

8. Improvement of the operation sequence

The basic sequence was written some years ago by the former group members. Since this version, only small changes were implemented, for instance the number of repetitions of the readout were changed for different measurements, and the exposure time was changed. For the improvement of the measurements, I amended the sequence.

8.1. Exposure time

The exposure time is set by a loop over 7 extra words, with a change of the number of loops and the wait time to change the exposure time. The longest hold time possible with one command is when doing 4095 cycles and 4095 hold time, which leads to an exposure time of 2.7 s. To increase the exposure time further, the command can be repeated.

In order to increase the exposure time as simple as possible, an implementation of a loop over the wait command was added. That way, not only longer exposure times are feasible, but it is easy to write measurement series, where the exposure time increases by a set amount. The implemented loop is shown in Fig. 22.

43	LI			SADR	0 0 0 0 0 0 0 0 0 0 0 0 0 0 0 0 0 1 1 1 0 0 0 0 1 0 1 0 1 0 1 0	000070AA	000	170	7	512	1031	0	Wait	
44	ACC	1		DCLK	0 0 0 0 0 0 0 0 0 0 0 0 0 0 0 0 0 0 0 0 0 0 0 0 0 0 0 0 0 0 0 1	00000001	000					0	NR+1	
45	JCR	7	43	DCLK	0 0 0 0 0 0 0 0 0 0 0 0 0 0 0 0 0 0 0 0 0 0 0 0 0 0 0 0 0 1 0 1	00000005	02B					101011	Number of Repetitions, default 1	5
46	LI			DCLK	0 0 0 0 0 0 0 0 0 0 0 0 0 0 0 0 0 0 0 0 0 0 0 0 0 0 0 0 0 0 0 0	00000000	000					0	Reset NR	

Fig. 22: The newly implemented loop. This makes it possible to increase the exposure time significantly.

Line 43: The wait command itself is implemented by loading the data to the register pointed by operand value with the LI-command. This command is the SADR-command, which pushes the data to the Pattern RAM readout instructions stack. The data, the 0's and 1's, are the jump address (last 12 digits), and the number of words (next 12 digits).

In the next step the data and the jump address are translated in hexadecimal - in this case zero because no jump occurs. The next four rows are the address in the pattern sheet, the number of words, the number of cycles and the hold time.

Line 44: In order to implement a loop, a value that is increased until a certain value is exceeded is required. The value used is DCLK. The are not many possible registers, and all of them are in use. Some not only save a value, but as well have different functions and are not available for programming. The DCLK was used only for the number of repetitions and has no further functions. It is therefore a good register to use.

With the ACC-instruction, the value specified in the date - in this case a one - is added to the register each time this line is loaded.

Line 45: With JCR a conditional jump is executed. If the value of the DCLK register is smaller than the value in the data the jump to line 43 is triggered. In this example, the number of iterations is set to 5. The way this is implemented, it does not make a difference on whether 0 or 1 is written in the data.

Line 46: After the loop, the DCLK register is set to zero again.

8.2. Line wise clearing of the detector

Due to problems with the sequence, the clear of the charges from the detector was implemented in a block at the beginning of the sequence. A loop cleared every row of the detector consecutively. This caused the feature, that latter rows at the end of the sequence have significantly longer exposure times than the earlier rows, since with only 100 repetitions, the read out of the detector takes almost a quarter second. Based on this configuration, different exposure times on different pixels are available for the analysis of the single electron generation rate.

Naively, in the first try, just a clear order was implemented after the read out of a single line was done. While this resulted in a proper oscilloscope signal, no data could be taken. After some research, it was discovered, that the trigger of the last RNDR and the frame trigger must not be too far apart from each other to be received by the ADCs system. For this reason a clear after each pixel hiders the read out.

To negate this, I implemented a loop, that sends the frame trigger before the clear (Fig. 23). This loop is necessary, because the frame trigger needs to be sent only once per frame, while the clearing must be done every row.

74	JCR	7	76	LRW	0 0 0 0 0 0 0 0 0 0 0 0 0 0 0 0 0 0 0 0 0 0 0 0 0 0 1 1 1 1 1 1	0000003F	04C	0	0	0	0	1001100	If not last row jump
75	LI			SADR	0 0 0 0 0 0 0 0 0 0 0 0 0 0 0 0 0 0 0 1 0 0 0 0 1 0 0 1 1 0 1 1	0000109B	000	155	1	0	20	0	Send Frame Trigger
76	LI			SADR	0 0 0 0 0 0 0 0 0 0 0 0 0 0 0 0 0 1 1 1 0 0 0 1 0 0 1 0 1 1 0 1	0000712D	000	301	7	0	80	0	Clear Pixel
77	NOP				0 0 0 0 0 0 0 0 0 0 0 0 0 0 0 0 0 0 0 0 0 0 0 0 0 0 0 0 0 0 0 0	00000000	000	0	0	0	0	0	
78	NOP				0 0 0 0 0 0 0 0 0 0 0 0 0 0 0 0 0 0 0 0 0 0 0 0 0 0 0 0 0 0 0 0	00000000	000	0	0	0	0	0	
79	LI			DCLK	0 0 0 0 0 0 0 0 0 0 0 0 0 0 0 0 0 0 0 0 0 0 0 0 0 0 0 0 0 0 0 0	00000000	000	0	0	0	0	0	Reset **NR**
80	ACC	1		LRW	0 0 0 0 0 0 0 0 0 0 0 0 0 0 0 0 0 0 0 0 0 0 0 0 0 0 0 0 0 0 0 1	00000001	000	0	0	0	0	0	**Row Counter +1**

Fig. 23: The newly implemented line wise clear, with the correct frame trigger.

Line 74: With the JCR command, the next line is skipped, unless the last line of the sensor is reached.

This jump is executed unless the row number in register LRW reaches 63, as defined in the binary data. The number 63 is used instead of 64, since the increase of the row counter happens after this loop at line 80.

Line 75: The frame trigger, which is written in the pattern RAM is sent after the last row is read out. This is done by loading the data with LI in combination with the execution of the pattern sheet commands with LI and SADR. Due to the previous line, this does not happen for other rows than the last.

Line 76: The current row of pixels is cleared with the SADR-command. This happens every row. In the last row, the clearing of the last line happens after the frame trigger is send.

77 & 78: No operation due to NOP.

Line 79: The date of DCLK is loaded with LI and set to the same value as is written in the binary data, which is zero. In other words, the counter for the number of RNDR cycles is reset.

Line 80: With the ACC-instruction, the value written in the binary data, which is one, is added to the LRW register. This means the row counter is increases by one.

9. Design of new and improved parts

Both to improve the setup, and to be able to use new detectors, some of the parts in DANAE had to be adapted. For this purpose, they had to be revised and redesigned.

9.1. Improving the shielding

As discussed in section 6, the detector is embedded in two layers of shielding, with a hole in each layer, to enable light from a LED or radiation from an iron source to illuminate the detector.

The holes however do impede the effectiveness of the shielding. For runs, in which no light from a LED is needed, it would be beneficial to be able to plug these holes. The CAD of the plugs (Fig. 24) fit smoothly in the holes of the shielding.

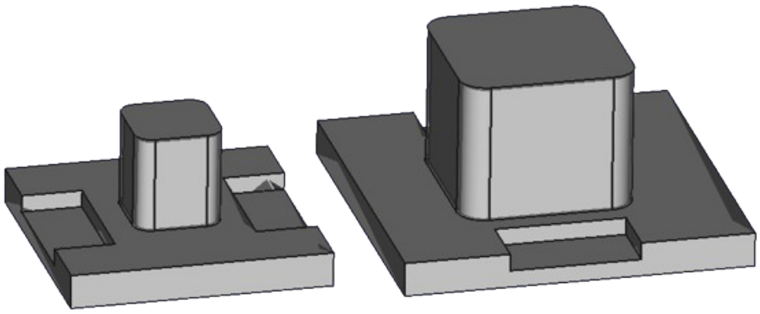

Fig. 24: The CAD for plug for the inner shielding on the left, and the outer shielding on the right.

The cap will be on top in the setup and prevents the plug from falling inside. The indents at the side of the cap are for easy handling of the plugs. With them, they can be inserted and removed without the need for tools.

9.2. Redesign of the frame for the readout board

The ROB is not directly fixed on the shielding, but instead it is fixed onto a frame. For the new detector, a new frame was needed. Unfortunately, the original design of the frame was lost, and only a preliminary model, that did not fit was available. The CAD of the frame is shown in Fig. 25.

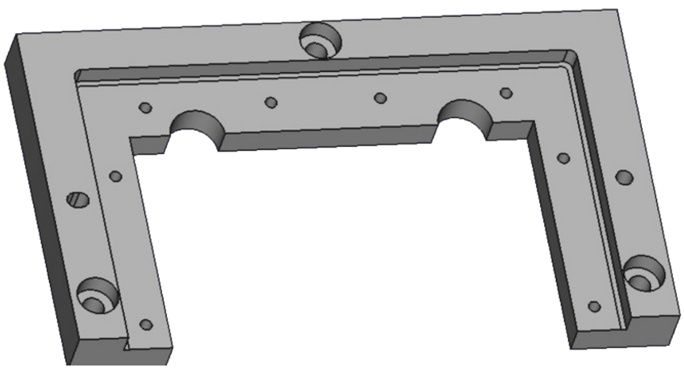

Fig. 25: The CAD for frame for the ROB with with the right measurements.

The preliminary model had the wrong measurements for the ROB, and the placements for the screws where missing, as well, which threads the screws need. The design was modified, such that the ROB fits, and the correct placement and size for the screw holes was determined.

9.3. New design of the frame

Currently, each detector has its own ROB attached to it via a flex PCB. To increase the active detector mass, several sensors will be used simultaneously in future setups. To test the response of different detectors and to catalog differences between the detectors, several of them need to be tested.

The resources needed can be greatly reduced by not using a separate ROB for each detector. Additionally, it is possible that each ROB has a slightly different response. When characterising behaviour of the different detectors, ideally all other variables should be the same. Thus, a reduced number of part needed for a new detector reduces the number of potential error sources. This limits the number of bugs, as well as decreasing the amount of time needed to find the mistake.

For these reasons, the group, in collaboration with the HEPHY technicians designed a modular detector concept, with one fixed ROB and a plug. Each detector can be plugged into the ROB.

Due to space restraints inside the vacuum chamber, the ROB with the plug cannot just screwed onto the outer shielding as it was done with the prior setup. That way, the flex-PCB from the outside could not be plugged into the ROB (Fig. 26).

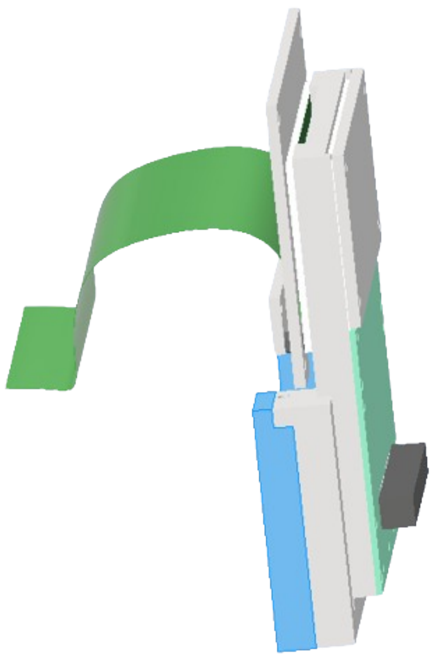

Fig. 26: The new modular design. The blue coloured part is fixed to the outer shielding, while the remaining parts can be fixed on top of it. The green flex- PCB is connected with a plug to the ROB.

Instead of fixing the frame for the ROB, an attachment is screwed to the outer shielding. The ROB shall be fixed on it from the top, after the flex-PCB that connects to the outside is fixed to it. Since the screws are tightened form the top, less space is needed to be able to manoeuvre.

The flex-PCB, which provides the connection to the detector is displayed in green. The large rectangle attached it to the plug to connect the detector to the ROB. This connection is used to plug different detector to the ROB.

9.4. Redesign of the outer shielding for the new setups

The new modular design needs more space than the prior design overhead. With the new connector, the flex-PCB became larger in vertical direction. This collides with the current thermal shielding.

In order to fit, part of the outer shielding needs to be removed. After taking measurements of the plug, and how the plug is fit onto the ROB, the excess material from the top part of the outer shielding was removed (Fig. 27). With this additional space, the increased size of the new setup fits.

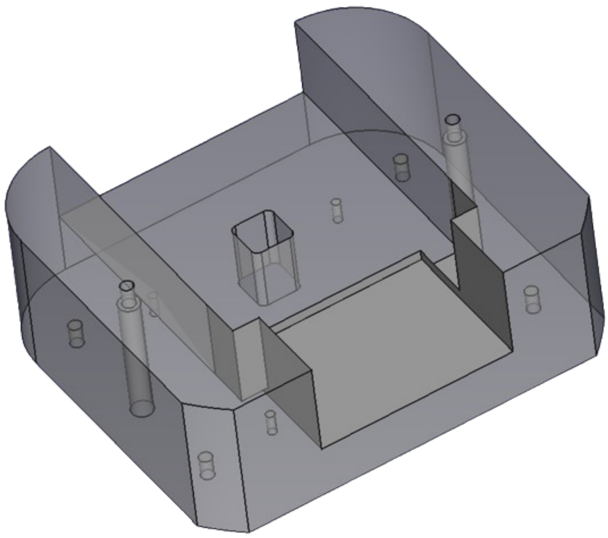

Fig. 27: The CAD for the upper, outer shielding block for the new setup.

10. Installation of the new detector

Since the detection of dark matter requires sensitive detectors, even minor effects of the RNDR DePFETs should be considered. To do this, a new detector is set up and calibrated. This is necessary, to understand differences between detectors for future expansion of the experiment using multiple sensors at once to increase the sensitive volume.

In this concept, the sensors are connected by using a BUS-System. For this purpose, it is necessary to be able to operate the different chips with similar voltage and current settings. The difference of thermally generated electrons will be studied as well.

10.1. The components

The sensor itself is fabricated by the *Halbleiterlabor der Max-Planck-Gesellschaft* (Semi Conductor Laboratory of the Max-Planck society, HLL) in Garching, Germany. The HLL is a specialised laboratory to fabricate scientific radiation detectors that are not commercially available [38].

The detector is connected to the readout board, which acquires the data. For the original ROB, the design for a different experiment was modified, but the modifications where not properly documented. Due to the missing changes, the detector did not work at the first try to turned it on.

From the manuals of the Veritas 2.1 and the SwitcherS, it became clear, that some of the bonding needed to be changed. The setup used for DANAE uses the drain current readout mode, while the bonding was for the source follower mode. For further differences, the circuit diagram shown in Fig. 28 was used.

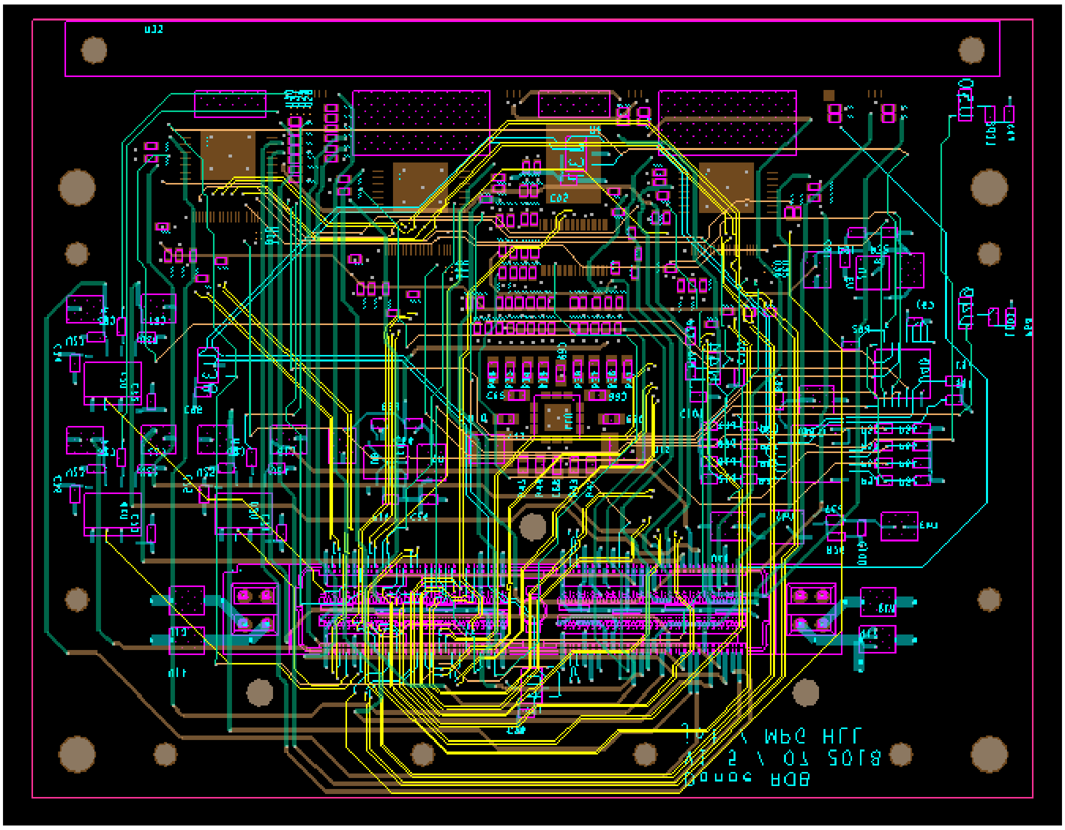

Fig. 28: The circuit diagram of the ROB with most of the layers visible.

10.2. Troubleshooting

Apart from the circuit diagram, important tools are the manuals of the individual components, as well as a microscope. With this, it became possible to inspect both differences between the circuit diagram and the ROB, as well as differences between the old and the new board. Measurements of the voltages and currents revealed a short cut to ground due to the mechanical structures as well.

Short between ROB and frame

At first, it was not possible to apply all the voltages without currents hitting the threshold. The transfer gate voltage was shorted with ground.

The problem was caused by a non-intended connection between the board and the metal frame, on which the board is fixed. This was repaired, by fastening tape on the metal edge of the ROB, as shown in Fig. 15.

Wrong bonding

The current for the V_{DD} voltage was consistently very high and the detector did not send a signal. Some tests were performed, and it was established, that the SwitcherS's are working.

Next, the ROBs of the new and the old module were examined and compared with a microscope. This revealed that the bonding of the Veritas and the switcher differs between the two modules. By consulting the Veritas 2.1 manual it was discovered that the bonding for the source follower mode was used instead of the bonding for the drain current read out mode.

Differences as seen by a microscope

When the new setup still did not work properly, the whole of the two boards was scanned with the microscope. Automatic scanning and image stitching was done, creating a mosaic of single pictures, with a total size of the resulting *.png* file of more than $500\,\mathrm{MB}$. In this picture, each component is displayed with high enough resolution to check whether it is the right one an is connected correctly. The placement between each one can be check.

Some differences were found. While some of them where of no impact, some missing components caused problems. A solder jumper had to be set at the Switcher west. This is a connection between to conductors. A resistor was missing as well, leading to a missing contact.

Measuring currents and Voltages on the ROB

Next, a new flex-PCB was build, to be able to measure the board when in use. The flex-PCB is necessary for this, because inside the vacuum chamber is not enough space to measure any components with outside measuring tools.

A voltage regulator, that should to change the $5\,\mathrm{V}$ supply voltage to $3.3\,\mathrm{V}$ did not work. The output was still $5\,\mathrm{V}$. After changing the defect component, the output is $3.3\,\mathrm{V}$.

Part III: Results

11. Analysis of the data with ROAn

While taking measurements, large amounts of data are generated. A measurement series over the weekend resulted in a dataset in the order of $500\,\mathrm{GB}$. The analysis is done with a framework called *ROOT based offline and online analysis* (ROAn). This software already existed but was modified by the group to meet the specific needs of repetitive readout like the data taken with DANAE.

ROAn is based on ROOT and is programmed in C++. ROOT is a software developed by CERN for the analysis of particle physics experiments, and "includes various statistical packages for the scientific analyses and visualization of large amounts of data" [39]. The analysis is done in multiple steps, and generates corresponding outputs. The individual steps and the results are described below.

11.1. Composition of the data and first quality control

The data acquisition is done with a *.bin* file as an array, in which each entry is a 16-bit number and corresponds to a complete row of the sensor. The total number of rows is 64 for the current sensor of DANAE. Each line starts with 4 entries, that are not important for the analysis. This is followed by 64 entries, followed by 3 further entries. The first 64 of these are the data taken by 64 columns, followed by a frame key, the number of the row N_{Row} and the number of the repetition N_{Rep}.

The frame key is one of the two highest values possible, either $2^{16}-1$ (65535) or $2^{16}-2$ (65534). As this value corresponds to the overflow bit of the ADC, no measurement of interest results in these values. This enables the analyses software to determines the frames by searching for the highest numbers.

In a first step of the analysis, the distance between entries with the value $2^{16}-1$ is checked. If the distance between two positive frame keys does not have the right dimension, the data in between those frame keys are rejected. This happens if a row is dropped for some reason or the full frame could not be recorded by the ADC. This usually happens at the beginning or end of the readout as well, unless the readout starts and ends exactly between frames. Another possibility is, that the signal is high enough, that the maximum value is recorded.

However, the data usually do not start and end with a frame, because they are not directly saved to the computer. Instead, the readout board has a memory buffer itself. The data are rather saved there until the buffer is full, before they are transferred to the PC. This means, that often the beginning or end of a frames are missing. This does not correlate with the length of the measurement compared to the exposure time, but only with the size of the data of each measurement.

The corrupted frames with missing end or beginning are rejected, as well as frames, in which data are dropped or added, by malfunctions of the electronic. The number of frames per buffer changes with the storage space needed for each frame. For instance, measurement employing 100 repetitions takes less space, than a measurement with 400 repetitions.

The data for each row are saved in an $N_{Column} \times 2 \cdot N_{Rep} \times N_{Frame}$ - matrix, where N_{Column} is the size of the detector. The detector in the current setup has 64 columns. N_{Rep} is the number of repetitions, or the number of readouts of each pixel. The factor 2 is due to the fact, that each pixel is constructed from two subpixels (section 4.4). The third dimension of the matrix is the number of the frame N_{Frame}. This is visualized in Fig. 29.

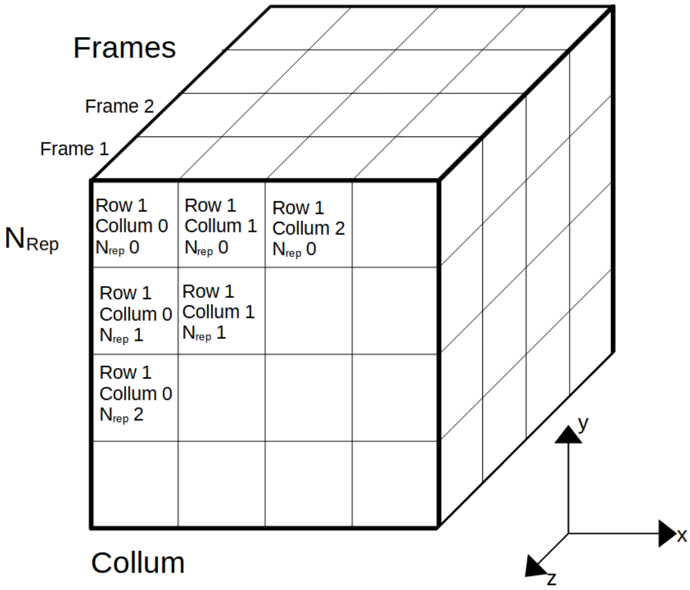

Fig. 29: The visualisation of the array for row 1. Each slice of the cube are all the values for a single pixel. For each measurement, there are 64 such cubes.

11.2. Offset correction

If no event is detected or the sensor is not exposed to any signal source, the recorded data reflect this by collecting noise values, ideally zero. However, usually instead there is a large offset, in order to enable the ADC to record negative values, as well. This offset is not constant and changes for different temperatures and voltages of the detector.

Since each pixel is expected to not detect an event most of the time, it should be empty and ideally display values centered around zero. To achieve this, an offset correction is needed. To correct for the offset, the mean over the repetitions and frames is taken. This is a slice of in the y-z plane of the data cube displayed in Fig. 29. This mean calculated is subtracted from each individual data entry. The data is then centered around zero. This correction is useful as well, to be able to compare the data for different measurements. After the correction, the data for each run are normalised. No extra conversion must be done to be able to compare different runs anymore.

11.3. Common mode correction

The common mode is a signal that is added due to the coupling of different electrical components at one point time. Since each row is read out parallel at one point in time, the common mode correction effect for each row is the same.

As a correction, the mean of each row over all its 64 pixels and N_{rep} repetitions is calculated and subtracted from its row. This corresponds to the one layer in the x-y plane of the data cube in Fig. 29. Without this correction, there are steps in the data as seen in

Fig. 30a, arising from periodic noise components. When the common mode is corrected, these artificial steps between lines vanish and the date become more uniform (Fig. 30b). Genuine events are still visible, meaning those are not filtered out.

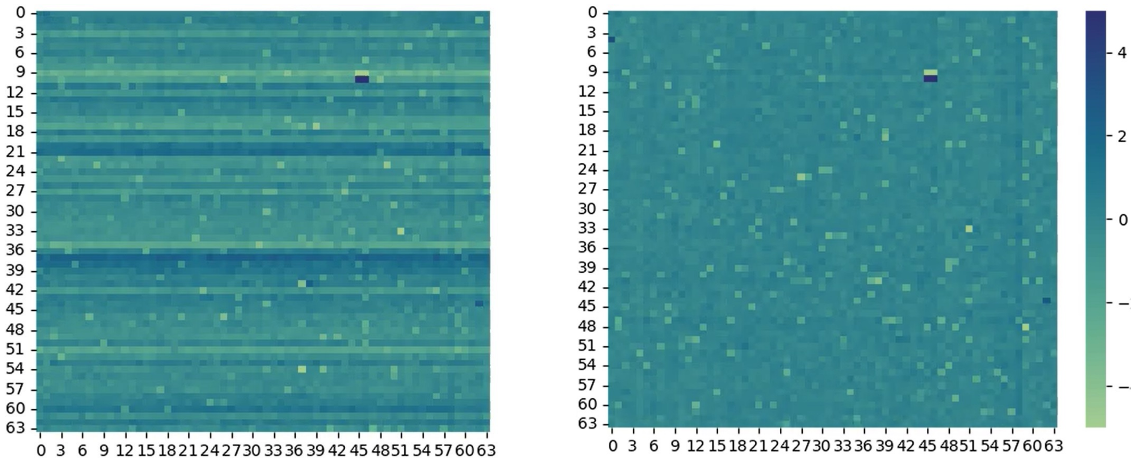

(a) The raw data taken is displayed without common mode correction.

(b) The same date is displayed with corrections for offset and common mode.

Fig. 30: The same date with and without corrections. The common mode interference is clearly visible as lines for each row.

11.4. Slopes of the RNDR readout

The data for each pixel in each individual frame are plotted against the number of repetitions. This corresponds to a single line on the y-axis in Fig. 29. For each frame 4096 such plots are generated. One of those plots is shown in Fig. 31a.

A linear fit is calculated for each of these plots. If no electrons are lost during the readout, and no events are detected during the RNDR, the gradient of the fit is ideally zero, apart from noise. After a histogram with the slops for each pixel and every frame of the measurement is created (Fig. 31b), it reveals that the entries are normally distributed. Every pixel whose slope is different can be assumed to lost or collected an electron during the readout process and is discarded. The threshold to identify these events is 5σ.

By dropping the pixels with too high slope values, bad pixels are ignored. Those pixels would disturb the further analysis and event maps.

11.5. Noise map

The corrected and filtered data of each pixel are displayed in a two dimensional histogram, called the noise map (Fig. 32). The data is the value of each pixel at each frame averaged over its repetitive readout.

The histogram displays the data in the x-z plane of the data seen in Fig. 29, but each value is averaged over the y-axis.

When no events are detected in the pixel, the measured values follow a normal distribution. The red line is the Gaussian fit for the histogram. The data for all the 4096 pixel are combined in a single histogram, (Fig. 33). The y-axis is the number of pixels in that bin, while the x-axis is displayed in arbitrary units of the ADC called *analogue digital unit* (ADU).

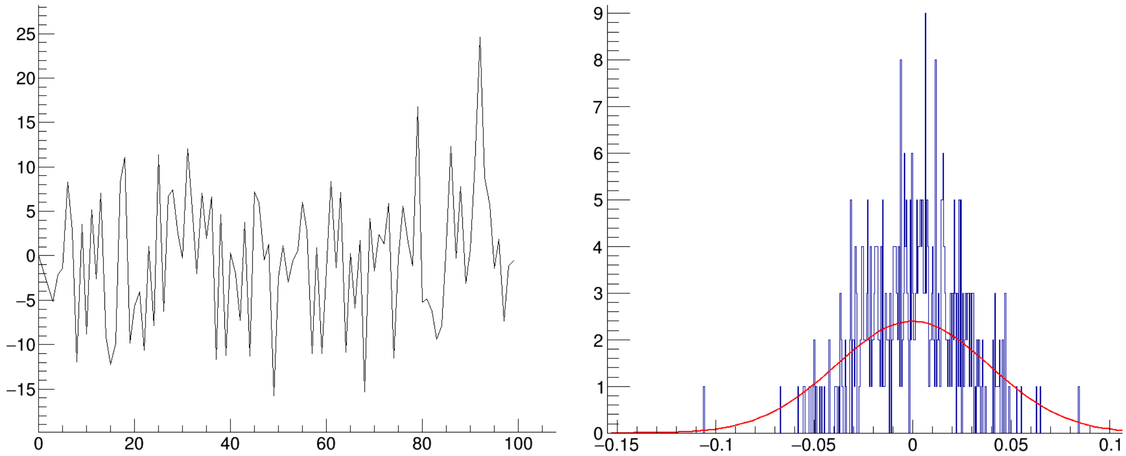

(a) The measurements for one pixel for each frame. The measured value is plotted against the repetition number.

(b) The slopes of one pixel with the Gaussian fit.

Fig. 31: a) For each pixel and each frame a plot for each measurement is generated. A linear fit is calculated, and in b) each slop is displayed in a histogram. The distribution of the slopes is normal, so a Gaussian function is fitted. All pixels with a slop that diverges by more than 5σ is dropped.

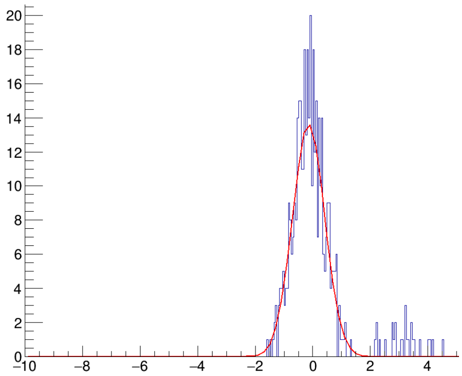

Fig. 32: The noise map displayed for a single pixel. There are 4096 such histograms for a measurement.

Not only the eventless occurrences are normally distributed. Rather this is as well the case for one electron events, and two electron events and so forth. However, the peak height gets lower and lower, as more electrons come together in on event. At least three peaks are visible in Fig. 33b, while only the *single electron event* (SEE) peak is clearly discernible in Fig. 33a.

If the peaks are sharp enough and the signal is generated by thermal excitation, their height follows a Poison distribution. The expected value is very small, such that the maximum is at zero, and the following peaks are very small.

11.6. Event map

A Gaussian fit is applied to the data from Fig. 33 for the pixels with no event. Every entry that exceeds 5σ of the fit – or the noise value – is counted as an event. This includes not only SEE, but those with two or more electrons as well.

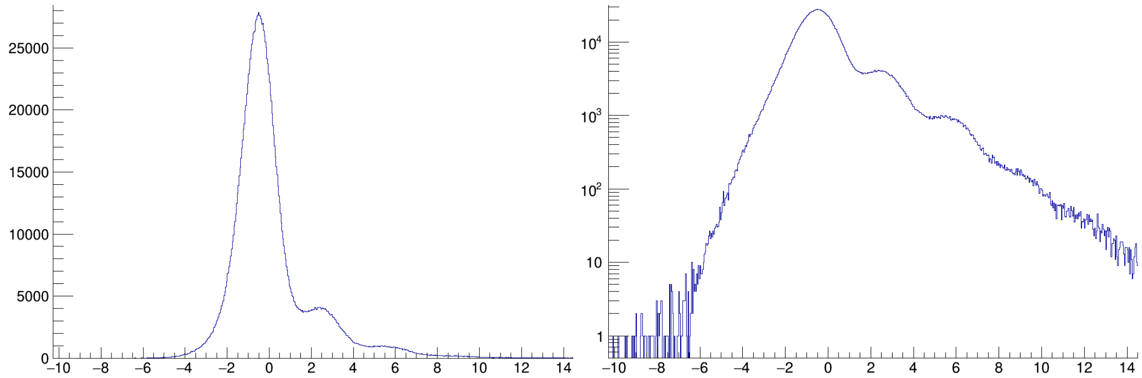

(a) The noise map histogram.

(b) The same noise map histogram. The number of entries is logarithmic.

Fig. 33: The data from all pixels are added up and displayed in a histogram. Du to the fact, that there are 4096 pixels, the noise is suppressed by a factor of 64. The form of the plot is much better visible. The date is shown without distortion in a), and with a logarithmic axis in b).

The map shows all events, that occurred during the measurement, including all frames that are not skipped in the quality control. When studying the event map of enough frames, possible defective pixels can be exposed, for instance dead pixels that never show an event. Another possibility are hot pixels, that often show an event, even if nothing has occurred.

Such an event map was created for each frame as well. However, in many frames, not a single event is detected. However, the total number of events is the crucial number. The study weather dark matter is responsible for some of the events or not is done by statistical analysis of the one electron, two electron and three electron events. This requires an extensive large data set.

11.7. Event tree

When the detector interacts with dark matter or any ionizing source, electrons are generated, that can be read out as a signal. However, most events might involve more than one electron and are not necessarily centred to the middle of one pixel. Electrons, which are generated at the edge between two or more pixels do not necessarily accumulate in an individual pixel. Instead, one single event can produce a signal in multiple neighboring pixels, not just in one pixel.

Multiple electrons are only able to disperse into different pixels, if the event occurs on a shared border. Therefore only the patterns shown in Fig. 34a are counted as one singular event. The patterns in Fig. 34b however are counted as more than one event, as are many others.

The clustering of multiple pixels to one event is only possible, because events are so rare. Most frames do not have a single event. This means, that the patterns from Fig. 34b are seldom witnessed either. If the clustering step is skipped, the number of events would be greatly exaggerated.

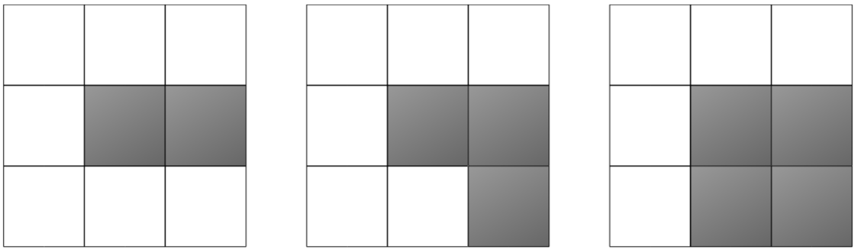

(a) This patterns are counted as one event. Apart from rotation, this are all possible pattern.

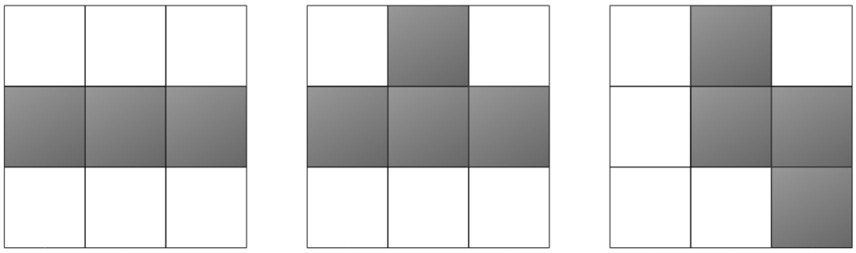

(b) This are some of the patterns that are not counted as a single event.

Fig. 34: Possible patterns of events in the event map. In a), those events are counted as one event, and the individual values are added together. The events in b) are not counted as a single event.

11.8. Gain map

During this step of the analysis, all the pixels where events occurred are known, as are the number of events per pixel. Equipped with this knowledge, the algorithm calibrates the events. After this step, no random values are displayed, but instead they are calibrated to electrons or any other physical value. The SEE are displayed with a magnitude of one, those events with two electrons have a magnitude of two and so forth.

12. Results from a temperature and exposure sweep

The further analysis was done with a Python script on JupyterHub on the CLIP-server[2]. For this, the ROOT files generated by the ROAn analysis software (see section 11) are used. To be precise, the event maps were used. The map for a temperature of $T = 160\,\mathrm{K}$ and an exposure time of $t = 170\,\mathrm{ms}$ is shown in Fig. 35.

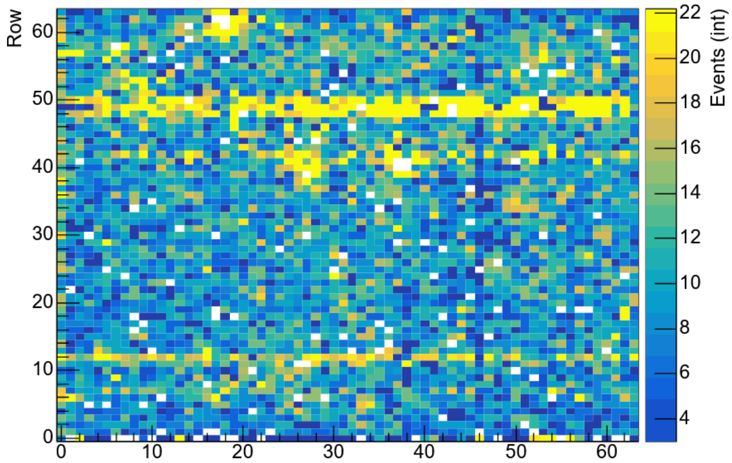

Fig. 35: The Eventmap of one Measrument.

To extract the single electron event rate depending on the temperature, multiple measurements were taken at each temperature with different exposure times. The temperatures of the cryostat range from $(70 - 150)\,\mathrm{K}$ and are separated by $10\,\mathrm{K}$ each. PT1000 sensors at the inner shielding determined the temperature of the detector to about $20\,\mathrm{K}$ above the set temperature of the cryostat. For the temperature sweep presented in the following, the number of repetitions is 100, resulting in 200 signal samples.

In a first step, a list is generated, in which all the file names are written. Then the event maps for all measurements are loaded into an array. Each measurement is composed of several frames. This number is different for each measurement, because corrupted frames were already skipped. The total number of events is divided by the number of frames in the measurement to normalize it to events per seconds.

The two pixels nearest to the edge of the detector are dropped, because of edge effects. As the electric field on the edges and charge sharing processes are different to the inner pixels, their data are not representative for the sensor. Instead of $64 \times 64 = 4096$ pixels, only $60 \times 60 = 3600$ pixels are examined.

The average is taken for each row. This is because for this sweep, the DePFET detector was cleared just once after each frame. Each row therefore has a slightly different exposure time. The number of events per pixel is plotted against the exposure time for each temperature, as shown in Fig. 36.

Each temperature has seven different exposure times for each frame. The exposure times set are $0.3\,\mathrm{ms}$, $85\,\mathrm{ms}$, $171\,\mathrm{ms}$, $236\,\mathrm{ms}$, $338\,\mathrm{ms}$, $503\,\mathrm{ms}$ and $671\,\mathrm{ms}$. The readout of each frame itself takes $305\,\mathrm{ms}$. This means, that the exposure times for some rows overlap (Fig. 36a), especially for the $170\,\mathrm{K}$ measurement. For this measurement, there are some errors leading to massively more events for the first measurement, such that the different measurements to not merge. Instead they are stacked above each other.

[2]The computational results presented were obtained using the CLIP cluster (`https://clip.science`).

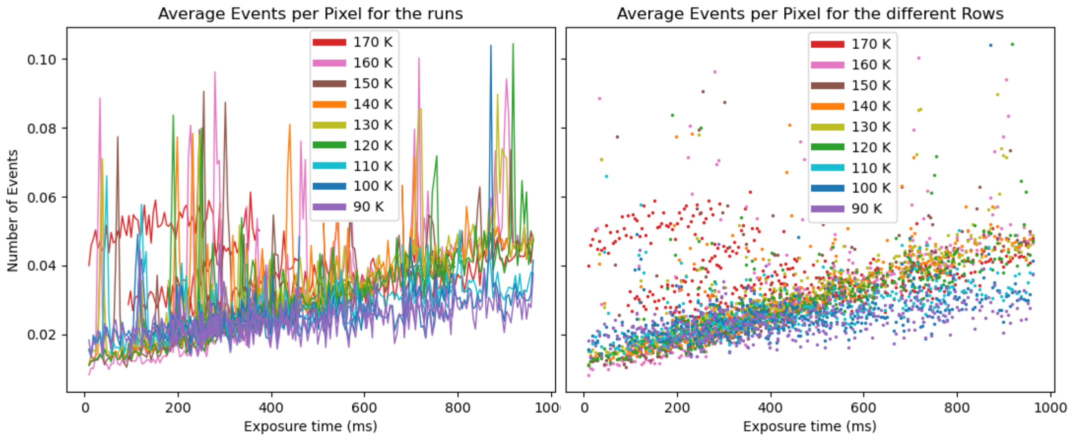

(a) The row wise number of events as a plot.

(b) The number of events as a scatter plot.

Fig. 36: The row wise number of events plotted against the exposure time for the different temperatures.

12.1. Selection and correction of the data

As seen in Fig. 36, the run at the warmest temperature of 170 K is visibly off, especially for low exposure times. Maybe the detector temperature was not jet in equilibrium or the was some disturbance on the detector. As this high temperature is not of interest for dark matter applications, this run will be dropped for further analysis.

Selecting pixels to drop

There are pixels that are overly exited or not exited at all. Those pixels have either very low or very high values. Those runaway values can be skipped to get results, which are representative for the sensor. First the mean of each measurement over all the frames is calculated, as well as its standard deviation. Secondly a mask is build. Each pixel that exceeds the the mean by two standard deviations in negative and positive direction is dropped. The graphs of the cleaned data is shown in Fig. 37.

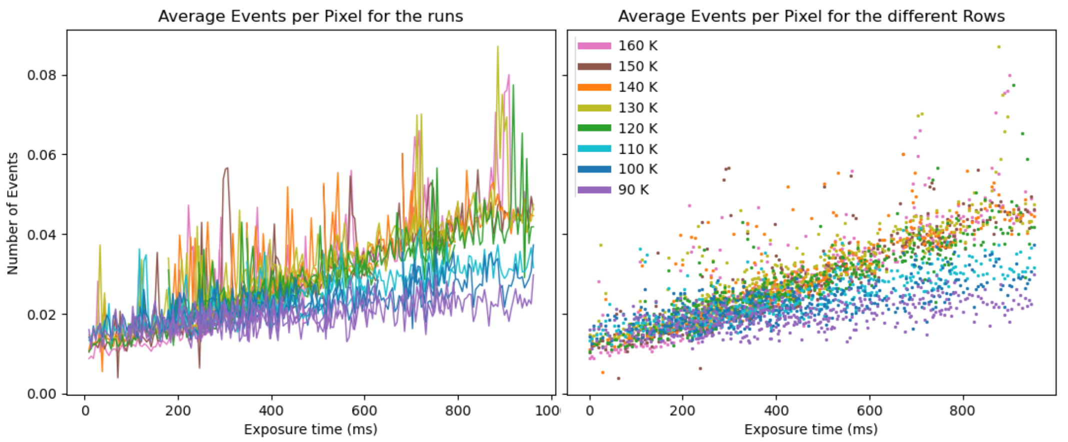

(a) The row wise number of events as a plot without the runaway values.

(b) The number of events as a scatter plot for the adjusted data.

Fig. 37: The row wise number of events plotted against the exposure time for the different temperatures. The bad pixels are dropped.

The adjusted data shown in Fig. 37 is a lot more tidy than the graphs in Fig. 36. There are a lot less blips, the maximum values are therefor decreased. That way, a single bad pixel does not mess up the average of an individual row. As a consequence, the accumulated values of one row is not divided by the number of pixels in the row, but instead by the number of approved pixels.

Discussion of the dropped pixel

The row and column or coordinates of the dropped pixels are saved. For each temperature and measurement an array is build. Each dropped pixel has the value one, while the good pixels are assigned to zero. The different maps of the different runs for one temperature are added together. A histogram of how often the same pixel is dropped reveals, that the majority of pixels affected in only one measurement. Those pixels are located within two to four columns (Fig. 38). The number of how often a pixel is dropped can be seen by the colour in the heat map for the temperature of 160 K.

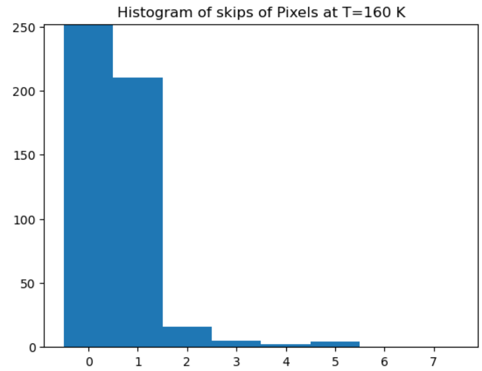

(a) Histogram of how often pixel where skipped. Note that the bin for zero times is cut off.

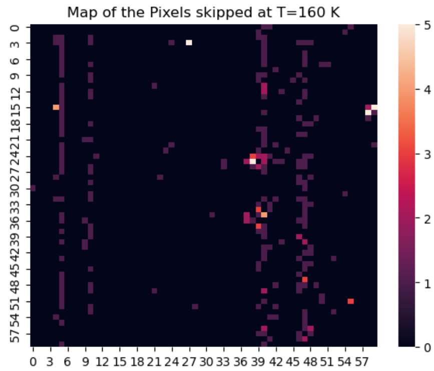

(b) A map of where pixels where skipped.

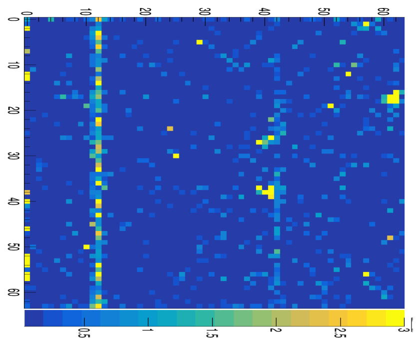

(c) A map where the analysis program had a bad fit, as described in section 11.5. The temperature of this measrumetn is 160 K.

Fig. 38: Visualisation of the skipped pixels. The amount of skips is displayed in a). In b) the skipped pixels are displayed in a map. In c) the bad fits are displays. Note, that this map is turned compared to the map in b).

While most of the pixels are only dropped in one of the seven measurement (Fig. 38a), the skipped pixels are not distributed randomly (Fig. 38b). Instead they cluster around certain pixels or rows.

In Fig. 38c is a map, showing where the Gauß fit described in section 11.5 had a bad fit. While the map in Fig. 38b has four lines, only two are present in Fig. 38c. However those are carried over to the skipped pixel map.

This map shows the skipped pixels of seven measurements, while the bad fit map only displays the bad fits of one measurement. The bad fits do not necessarily have to be on the same pixels for every measurement. The bad fits of explain the bad pixels.

12.2. Number of events

The amount of detected event varies, depending on the examined temperatures (Fig. 37), similar to the slopes of the number of events plotted against time. The total number of events detected is displayed in Fig. 39.

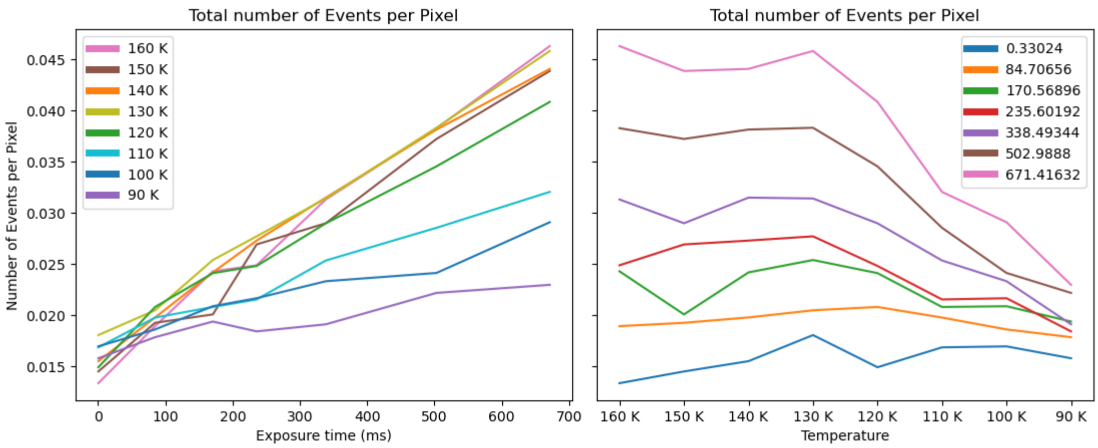

(a) The total amount of events detected in each measurement for the different temperatures.

(b) The total amount of events detected in each measurement plotted against the temperatures.

Fig. 39: The total average amount of events per pixel for the separate rows. A longer exposure means more events, an lower Temperature leads to less events.

For all temperatures, the number of events is directly proportional to the length of the exposure, as a longer duration for excitation of electrons is available. Due to the thermal excitation, lower temperatures lead to a reduced number of events. While there is a clear drop, contrary to the exposure time, the best way to fit the curve is not obvious.

The reduced amount of detected SEE is due to the fact that less dark current is generated at lower temperatures, which leads to an improved signal to noise ratio. The dark current expected is:

$$\frac{I(T_1)}{I(T_2)} = \left(\frac{T_1}{T_2}\right)^2 \cdot \exp\left(-\frac{E_{gap}}{2k_b} \cdot \left(\frac{1}{T_1} - \frac{1}{T_2}\right)\right) \tag{19}$$

Given a dark current $I(T_2)$ at temperate T_2, the dark current $I(T_1)$ at temperature T_1 is calculated with this formula. The only needed variables are the Boltzmann constant k_B and the energy of the band gap E_{gap}. The latter slightly varies for different processed and irradiated silicon.

The amount of dark current present drops exponentially with decreasing temperature. The detected amount of events drop with decreasing temperature (Fig. 39b). This drop is quite steep for temperatures lower than $130\,\mathrm{K}$. In addition to the dark current the SEE generation is as well affected by background radiation sources.

12.3. Events per unit time

A longer exposure times corresponds to a larger number of events (Fig. 37). The effect becomes visible in the rows for the individual measurements, as well as for the same row but with different exposure times. The data are fitted linearly to the formula:

$$D = s \cdot t + o \tag{20}$$

The data D is equal to the slope s times the time t plus the offset o. The time increment used is one second. The offset is discussed below. The slopes for the different measurements are shown in Fig. 40a, while the slop for the different rows between measurements are shown in Fig. 40b.

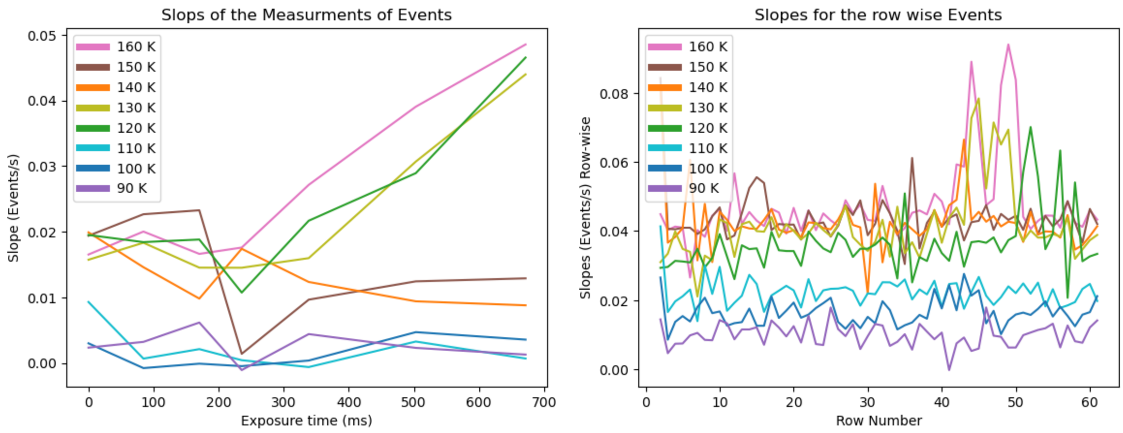

(a) The slopes for the different measurements. Each data point is the slop of one complete individual measurement.

(b) The slopes of the individual rows between the measurements with different exposure times.

Fig. 40: The slopes of the data for the temperature sweep.

The two ways of plotting the slops have distinct advantages and disadvantages. The slopes for the different measurements or exposure time (Fig. 40a) have the benefit of ignoring the offset of the individual measurements, by averaging over such a large number of pixels, that individual, defect pixels do not have a large impact. For example, the data with the shortest exposure at 170 K in Fig. 36a has a major offset, while the slope is about the same as for the other measurements at this temperature.

For the row wise slopes (Fig. 40b) the offset effects the data quite strongly. Because of the large offset for the first measurement, all the slopes for the individual rows are negative instead of positive. However, if only individual rows of the measurement are off, the slopes do not get disturbed as much as the slopes between the measurements. If the number of events where not plotted against the exposure time, but instead against its row number, most of the large outliers are on the same rows.

The slopes of the different rows are displayed in a histogram in Fig. 41a. This way frequent slopes are shown quite clearly, while singular outliers are easily spotted and neglected.

There is a clear trend, that a lower temperature corresponds to a smaller slope or thermal generation per time. In addition, less events are detected, therefore the slope is lower as well.

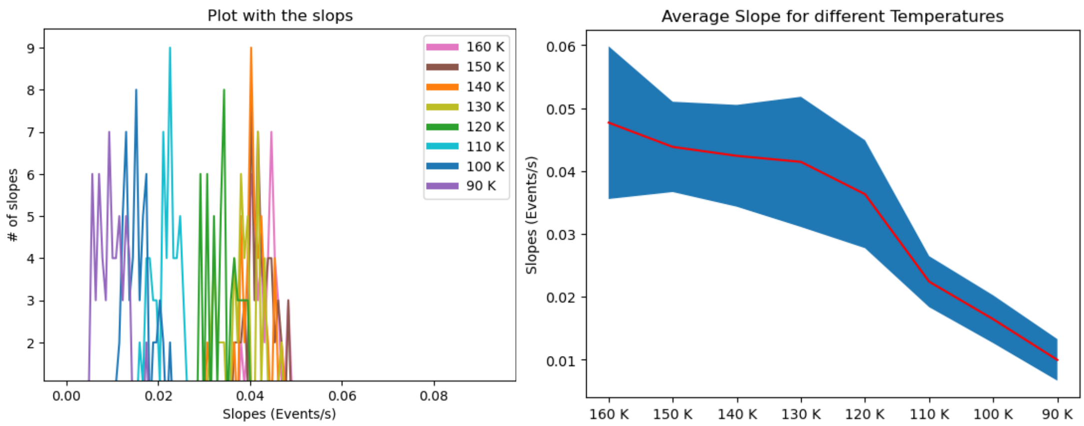

(a) Histogram of the slopes of the rows for the different temperatures.

(b) The average slope for the different temperatures.

Fig. 41: The slopes detected for the different temperatures, as both a) a histogram, as well as b) a plot with the one sigma uncertainty.

12.4. Offset

Fitting the different events per pixel from Fig. 37 in a linear fit with Eq. (20), results in the slope s, as shown prior and the offset o. The offset describes how much the fit is away from the origin, when the line crosses the y-axis at $t = 0$ (Fig. 42). Simplified the offset can be correlated to a non-exposure time dependent surface current generated by electric fields or switching processes, while the slope is correlated to a exposure time dependent bulk current generated by thermal excitation.

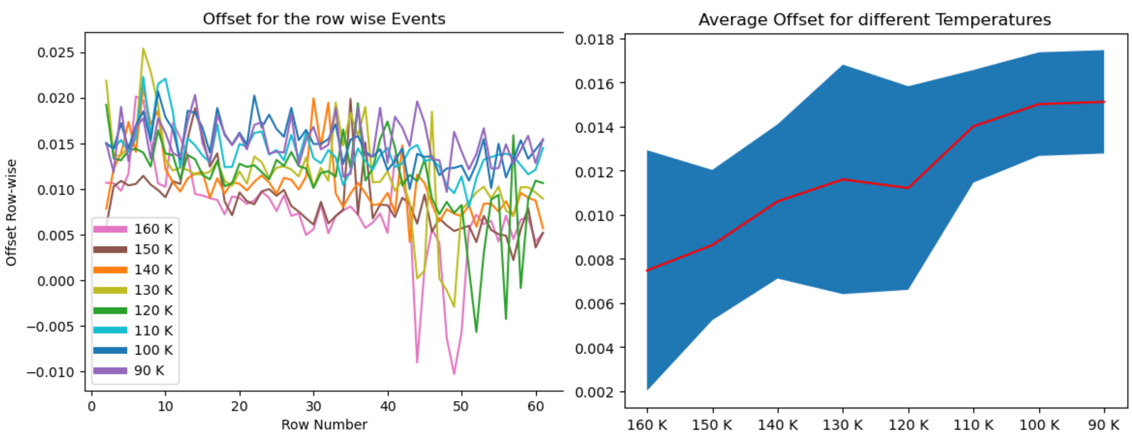

(a) The offset for the linear fit for each row between the measurement.

(b) The average offset of the different temperatures with the uncertainty.

Fig. 42: The offsets for the different temperatures.

The offset is the number of events detected, if the exposure time would be zero. The fits for the lower temperatures have a greater offset than the fits for the higher temperatures most likely due to the increased field free mean path. While the data is quiet noisy for each row (Fig. 42a), the picture becomes more clear when an average is taken for each temperature. The offset is plotted against the temperature, as displayed in Fig. 42b. The analysis of the offset is the same as for the slopes, however only the final result is shown.

12.5. Further interpretation using pixel-wise analysis

In the prior analysis, each data-point was calculated as an average over a row. That way trends are visible more easily in a single diagram and individual plots are not crowded. However, in order to facilitate a statistical analysis, a larger number of data-points is useful.

The number of events plotted against the exposure time is shown in Fig. 43, without displaying individual data-points (different to Fig. 37). This is due to the fact, that 60 times as many data-points are present for each measured temperature. The individual points in a scatter plot overlap such that there is one continuous area visible, and no trend can be discerned.

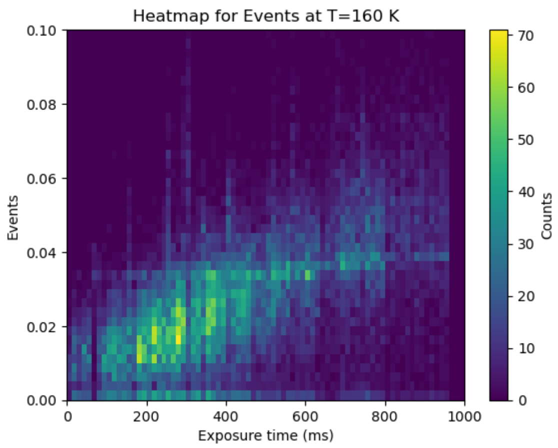

Fig. 43: The amount of events plotted against the exposure time at temperature $T = 160\,\mathrm{K}$.

Because, the individual exposure times overlap between different measurements, there are more events present for longer exposure times and more data-points are available. The same analysis as previously described was conducted to the the data of the individual pixels. The slopes and offsets between the same pixel with different exposure time is calculated for the 3600 pixels. The histograms for the slopes are shown in Fig. 44a.

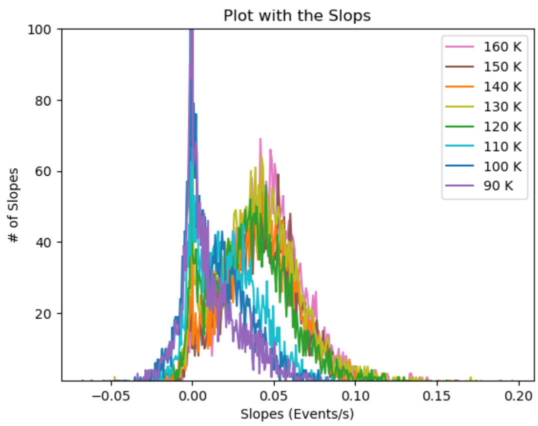

(a) Plot of the histogram of the slopes for the different temperatures.

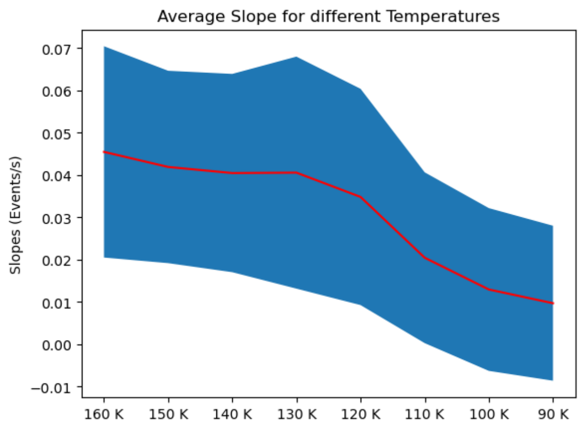

(b) The average slope plotted against the temperature.

Fig. 44: The slopes of the pixel-wise analysis.

The distribution of the slopes is Gauian, which is well pronounced in this analysis. The plot of the average slope for each temperature has the same shape. However, the noise is much larger than at the row wise analysis, which benefits from averaging the signals of one row.

The histogram and average offset for the analysis for the individual pixels is shown in Fig. 45. The shape of the histogram is Gaussian as well. There is an upwards trend of the offset for lower temperatures. However the uncertainty is much larger than the difference of the offset between different temperatures because the noise in the single rows is not ignored.

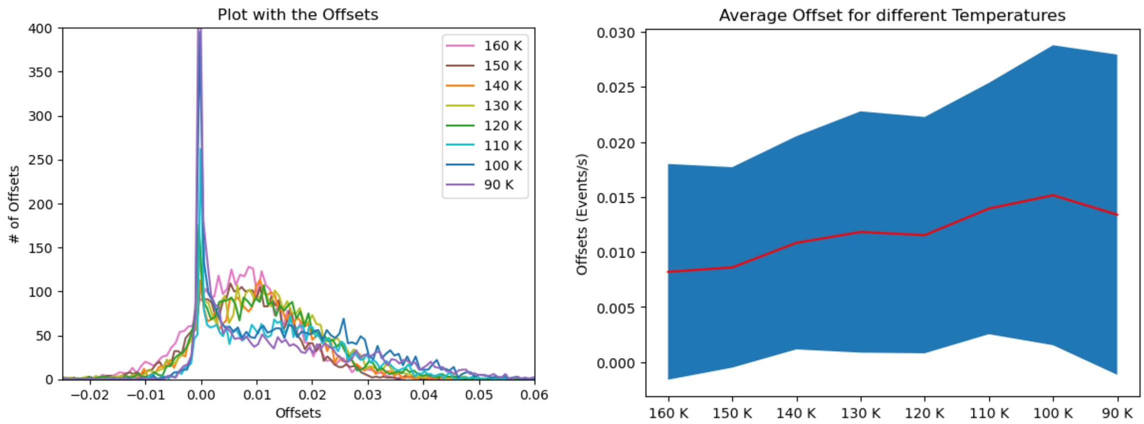

(a) Plot of the histogram of the offsets for the different temperatures.

(b) The average offset plotted against the temperature.

Fig. 45: The offsets of the pixel-wise analysis.

12.6. Discussion

From the data analysis presented in this chapter, some conclusions can be drawn. Firstly, a longer exposure time leads to more events. This is the case for all the measured temperatures, both in one measurement as well as between measurements with longer exposure times. This is visible both in Fig. 37, and in the slope analysis of the graphs in Fig. 40 and Fig. 41.

While longer exposure time leads to more events for all temperatures, the slope is not the same at different temperatures. This is best seen in Fig. 41. Higher temperatures lead to a higher number of events per second. In other words, the slope of the original plot in Fig. 37 is steeper.

Since the number of dark matter particles interacting with the detector is independent of the temperature of the detector, the increased slope is a detector property. It is due to an increased dark current. The actual number of events should therefore be lower.

Contrary, the offset, as shown in Fig. 42, has a higher value for lower temperatures. The difference however is less significant.

This can be seen, even though the results are quite noisy. Further data taking with a much larger number of frames would mitigate this to a certain degree. However, there are systematic errors as well. One such error is presented in Fig. 46.

Spikes in the average number of events corresponded more closely with the column number than the exposure time. This is due to hot pixels and hot rows. Those are pixels that generate much higher signals than normal pixels, due to some defect, either with the

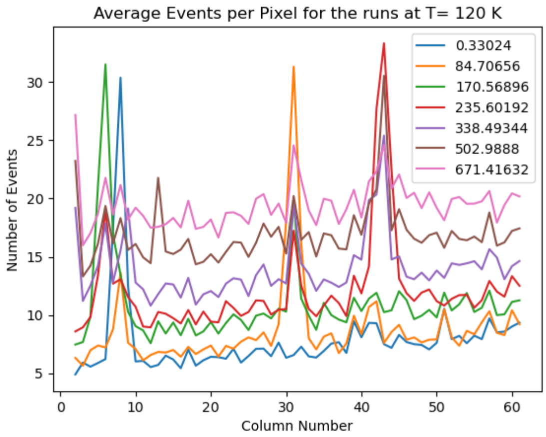

Fig. 46: The average number of events per Row for each column. The spikes ailing with the column number.

pixel itself, or with the readout of this pixel. However, this is mostly mitigated with the correction discussed in section 12.1.

Both for the value of the slopes and the offset, as seen in Fig. 44a and in Fig. 45a, there is a clear clustering around zero at low temperatures. This effect is so strong, that the maximum of the y-axis was limited in order for the other data to still be easily discernible.

The clustering around zero is due to the fact, that at lower temperatures, the transfer of the charges between the two internal gates of the DePFET in a super-pixel does not work as well anymore. The DePFET has a hard time detecting any events at all, even if they occurred, and charges are dropped during the RNDR. Do to the dropping, the peaks blur.

This effect can be seen in the raw data, as shown in Fig. 47. The amount of SEE detected is smaller, and the differentiation between the separate peaks is much smaller.

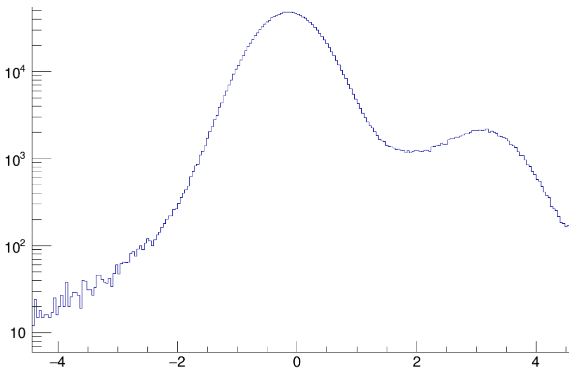

(a) The raw data of the the measurement at a temperature of 160 K.

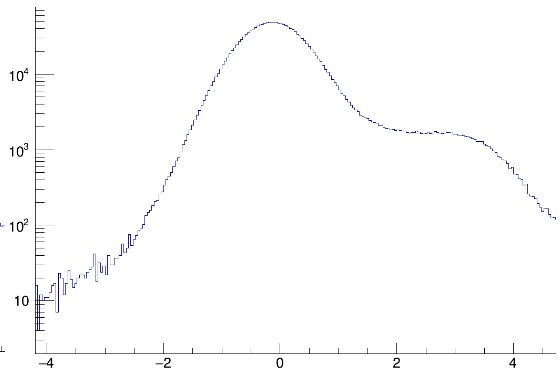

(b) The raw data of the the measurement at a temperature of 90 K.

Fig. 47: The raw data of the measurements at different temperatures with an exposure of 671 ms. The histogram displays how often a certain value was detected.

The ROAn analysis then has a hard time fitting the Gauß of the zero electron peak. The Gauß is frequently to wide, and events are ignored, leading to an even lower event count.

Due to the inflated number of zero events detected, there is an increased amount of fits for data, were each data point is zero. This leads to a perfect fit with both an offset and a slope of zero.

As shown in section 12.1, the pixels that are ignored due to being outliers, is due to the fact, that they have a bad noise fit. This is displayed in Fig. 48.

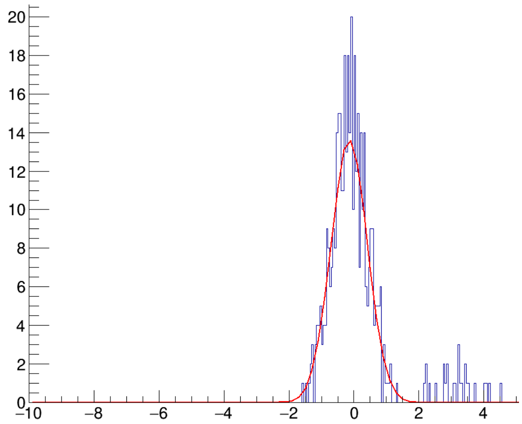

(a) A pixel, were the analysis of the noise worked.

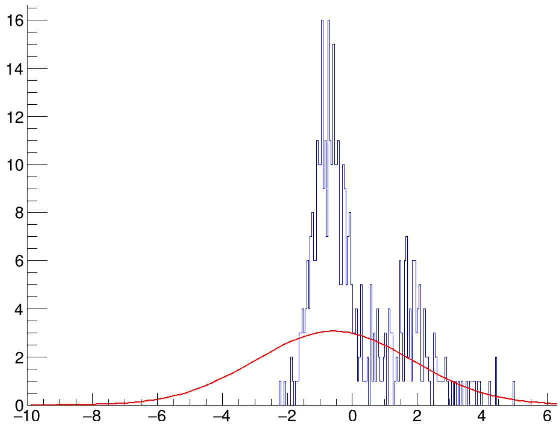

(b) A pixel, where the analysis failed.

Fig. 48: Shown are the noise analysis, as discussed in section 11.5 from two different pixels. One analysis work, the other failed.

The analysis of the pixel in Fig. 48a works well. ROAn is able to use a proper Gauß fit for the data, and the events are displayed correctly. In Fig. 48b however, the fit is bad. Both the peak for no events, as well as the SEE- peak are put under the same Gauß. The sigma of the fit is to large, and events are not properly detected. That leads to disturbed pixels, that detect events much to often or not often enough. That is the reason why the discarded pixels align with the pixels with large noise.

The SEE generation rate is about 0.02 events per second and per pixel in each frame for a temeprature of $110\,\mathrm{K}$. This correspondesn with one event detected every 50 seconds, and for and an exposure time of $338\,\mathrm{ms}$ one event about every 150 frames. The probability that two events randomly coincide is therefore $4.44 \times 10^{-3}\,\%$.

The events generated are not only the product of dark current. The setup is not properly shielded against radiation in this surface run. Therfor muons or gamma radiation does generate events as well.

13. Future prospects for DANAE

In order to prepare the scientific data taking for dark matter detection, the setup of DANAE has to be improved. A radio pure shielding has to be implemented to facilitate that the inside of the vacuum chamber becomes clear of all sources of radiation. In addition, the sensitive mass of the detector hast to be increased.

13.1. Shielding

Right now, there is no optimized shielding against radiation at DANAE. Shielding is important to get ride of events, that will result in SEE. This is mainly caused by radiation from radioactive decay of different atoms, or a number of elemental particles, such as muons.

The current shielding is the building of HEPHY and includes the vacuum chamber and the temperature shielding. The vacuum chamber protects the detector from temperature fluctuations, as well as α- and β-radiation. However the combined shielding does little against other sources especially cosmic radiation.

The proper thickness of lead for shielding needs to be simulated. Depending on the thickness, either the inside of the vacuum chamber has to be modified to be able to host the shielding. If the shielding is too thick, it has to be put up at the outside of the chamber. Either way, the stability of the table has to be checked, to exclude the possibility of an accident.

At the moment, both the inside of the vacuum chamber as well as the thermal masses for temperature shielding are made out of aluminum. However, aluminum has a low radiation purity, and is therefor not ideal for this purpose. Instead, radio pure copper should be used [40].

For this, all the different parts inside the vacuum chamber have to be reproduced with copper. While copper is radio pure, it is not ideal to be milled. This means all measurements of the components must be exact, such that no further milling is required.

After the experiment is finalised and tested, it will be moved to an underground location. This way, the rock and earth will provide further shielding against cosmic radiation.

13.2. Sensitive Mass

For dark matter detection, the sensitive mass should be as large as possible. That way, the rare interaction events happen more frequently. The increase of the sensitive mass is intended in several steps.

First, a second 64×64 sensor will be put in the setup. The second sensor will be read out at the same time as the first one to provide a combined signal. Effectively, this is still a 64×64 pixel matrix, but the sensitive mass of each pixel is doubled by pixel binning of both sensors. That way, nothing on the front end electronic side, like the readout has to be changed, only the wiring on the flex-PCB from the readout board to the detector has to be modified. In other words, both sensors will be operated by the same SwitcherS and Veritas ASICs.

Next, the two 64×64 sensors will be read out consecutively, effectively forming a 128×64 detector. For this setup, the steering or SwitcherS ASICs have to be modified in order to be able to read out 128 rows. This might be done with a single multiplexer current, which is, only switching between the first and second sensor or by including additional SwitcherS.

Then a 2×2 sensor matrix will be set up, yielding a 4 times larger detector volume with 128×128 pixels. For this setup, the ROB has to be partly redesigned. However, if done properly, it can be designed in such a way, that it is possible to increase the $N \times N$ detector matrix to arbitrary size.

The drawback of the last option is the increased readout time due to the rolling shutter operation. However, it increases with the square root of the number of pixels. Still, the size of the detector is not only limited by the amount of data created per time, and the physical size of the detector. The acquisition time should not be increased indefinitely.

13.3. Fine tuning

For all measurement setups, all the settings for the voltage and current have to be adjusted. This is not only necessary, when changing the whole setup, but when changing the measurement temperature as well. Especially very low temperatures, which are of high interest for dark matter searches require a specific adaption of the operation voltages in order to take into account the modified channel resistivity and material properties.

It has to be investigated, if it is necessary to change all the settings, as soon as the configuration will be changed for one 2×2 sensor matrix to another one. A drift over time is possible as well.

14. Conclusion

The goal of this thesis was, to modify the setup and operation of the DANAE setup, in order to increase its sensitivity for light dark matter. This is done by examining the working principle of the experiment.

To enable a flexible control of the exposure time of individual pixels, the sequence controlling the detector was modified to enable longer exposure times. Instead of a maximum of $2.7\,\mathrm{s}$, several hours are now feasible. Another change of the sequence regards the clearing of the RNDR-DEPFET pixels. Instead of clearing the hole detector at once, the changes enable a clearing sequence after the readout of each line. This way, the exposure time of the hole detector is the same, and no additional exposure time is added to each row anymore.

The design of the readout board was studied, debugged and documented. This resulted in the identification of errors and defective components, which were either fixed or replaced in cooperation with the HEPHY technicians. Parts of the setup were changed or added, such as plugs for the temperature shielding, which increased the shielding against background - including blackbody radiation - in case no radiation sources like an LED is needed. The frame for the ROB was redesigned, such that the new detector could be used in the experiment.

In order to enable the simple exchange of detectors in future, a new fixture for the ROB was developed. The different detectors can be connected to this ROB with a specific plug. That way, the same ROB will be used for different sensor modules. This reduces the amount of troubleshooting for a new detector and reduces the sources of errors by operating a well established ROB. This process required the redesign of the frame to fit into the available space inside the vacuum chamber together with a modification of the outer temperature shielding.

As soon as the hardware adaption was finished, a measurement series with varying temperatures and exposure times was performed over a period of four days. This duration is required to enable the large thermal mass of the setup to settle at a new temperature.

The acquired data were first analysed with a C++ software package called ROAn within a first step, to further process the results with a Python program. The analysis resulted in a generation rate between $(0.01 - 0.05)$ electrons per second for each pixel depending on the temperatures. As expected, the generation rate was not randomly distributed among the temperatures. Instead, the highest generation rate corresponds to the warmest temperature, while the lowest generation happens at the coldest temperature measured.

It was discovered, that for low temperatures the transfer of the electrons in the DePFET super-pixel does not work properly. As a result, the peaks for the number of electrons detected smear. Because of this, ROAn has problems discerning events from the background. To amend this, the operation parameter corresponding to the transfer of the electrons must be changed in future. This concerns the transfer voltage as well as the duration of operational steps, e.g. the time the transfer gate is turned on.

List of Acronyms

ADC	Analog-to-Digital Converter
ADU	Analogue Digital Unit
ASIC	Application Specific Integrated Circuit
ATHENA	Advanced Telescope For High Energy Astrophysics
BUS	Binary Unit System
CAD	Computer Aided Design
CCD	Charge-Coupled Device
Λ-CDM	Λ-Cold Dark Matter
CDS	Correlated Double-Sampling
CERN	Conseil Européen Pour La Recherche Nucléaire (European Organization for Nuclear Research)
CLIP	Cloud Infrastructure Platform
CMB	Cosmic Microwave Background
COSINUS	Cryogenic Observatory for Signals seen in Next- Generation Underground Searches
CP	Charge Conjugation And Parity
CRESST	Cryogenic Rare Event Search With Superconducting Thermometers
DAMA/LIBRA	Dark Matter Detection With A Large Sodium Iodide Bulk For Rare Processes
DANAE	Direct Dark Matter Search Using DePFET With Repetetive Non-Destructive Readout Application Experiment
DC	Direct Current
DePFET	Depleted p-Channel Field Effect Transistor
DM	Dark Matter
DR	Drain Current Readout
ENC	Equivalent Noise Charge
FET	Field Effect Transistor
FPGA	Field Programmable Gate Array
HEPHY	Institut für Hochenergiephysik (institude of high energy physics)
HLL	Halbleiterlabor der Max-Planck-Gesellschaft (Semi Conductor Laboratory of the Max-Planck society)
I^2C	Inter-Integrated Circuit
ILC	International Linear Collider
LED	Light Emitting Diode
MACHO	Massive Compact Halo Object
Λ-MDM	Λ-Mixed Dark Matter
MOND	Modified Newtonian Dynamics
MOSFET	Metal-Oxide Semiconductor Field Effect Transistor
EPP	Multi-Functional Board
N/S	Noise-to-Signal Ratio
PCB	Printed Circuit Board
QCD	Quantum Chromodynamic
RAM	Random Access Memory
RC	Resistor-Capacitor

RMS	Root Mean Square
RNDR	Repetitive Non-Destructive Readout
ROAn	ROOT Based Offline And Online Analysis
ROB	Readout Board
SDD	Silicon Drift Detector
SEE	Single Electron Event
SEU	Single Event Upset
SNR	Signal-to-Noise Ratio
SPI	Serial Peripheral Interface
SRAM	Static Random Access Memory
Veritas	Versatile Readout Based On Integrated Trapezoidal Analog Shapers
WIMPs	Weakly Interacting Massive Particles
ÖAW	Österreichische Akademie der Wissenschaften (Austrian Academie of Science)

References

[1] Riccardo Catena and Piero Ullio. A novel determination of the local dark matter density. In: *Journal of Cosmology and Astroparticle Physics* 2010.08 (August 2010), pp. 004–004. ISSN: 1475-7516. DOI: 10.1088/1475-7516/2010/08/004.

[2] L. Reuen et al. Performance of a DEPFET prototype module for the ILC vertex detector. In: *Nuclear Science, IEEE Transactions on* 53 (July 2006), pp. 1719–1725. DOI: 10.1109/TNS.2006.873079.

[3] T. S. van Albada et al. Distribution of dark matter in the spiral galaxy NGC 3198. In: *The Astrophysical Journal* 295 (August 1985), pp. 305–313. DOI: 10.1086/163375.

[4] Fritz Zwicky. The Redshift of Extragalactic Nebulae. In: *Helvetica Physica Acta* 6 (1933), pp. 110–127. ISSN: 0018-0238. DOI: 10.5169/seals-110267.

[5] John Kormendy and Ralf Bender. Supermassive black holes do not correlate with dark matter halos of galaxies. In: *Nature* 469 (January 2011), pp. 377–80. DOI: 10.1038/nature09695.

[6] Douglas Clowe et al. A Direct Empirical Proof of the Existence of Dark Matter. In: *The Astrophysical Journal* 648.2 (August 2006), pp. L109–L113. ISSN: 1538-4357. DOI: 10.1086/508162.

[7] Center for Astrophysics, Havard & Smithonian. Galaxy Clusters. URL: https://www.cfa.harvard.edu/research/topic/galaxy-clusters (visited on 12. 12. 2023).

[8] NASA/CXC/M.Weiss. More Images of 1E 0657-56. 2006. URL: https://chandra.harvard.edu/photo/2006/1e0657/more.html (visited on 12. 12. 2023).

[9] David Harvey et al. The nongravitational interactions of dark matter in colliding galaxy clusters. In: *Science* 347.6229 (March 2015), pp. 1462–1465. ISSN: 1095-9203. DOI: 10.1126/science.1261381.

[10] Hwang Ho Seong et al. Comparing dense galaxy cluster redschift survesys with weak-lensing maps. In: *The Astrophysical Journal* 797.2 (December 2014). DOI: 10.1088/0004-637X/797/2/106.

[11] European Space Agency. Planck and the cosmic microwave background. URL: https://www.esa.int/Science_Exploration/Space_Science/Planck/Planck_and_the_cosmic_microwave_background (visited on 29. 01. 2024).

[12] European Space Agency. Planck Power Spectrum. URL: https://www.esa.int/ESA_Multimedia/Images/2013/03/Planck_Power_Spectrum (visited on 29. 01. 2024).

[13] Mariano Ruben Cababie. Origin and characterization of single-electron events in Skipper-CCDs for the search of light dark matter. PhD thesis. Universidad de Buenos Aires, 2023.

[14] R. K. Sachs and A. M. Wolfe. Perturbations of a Cosmological Model and Angular Variations of the Microwave Background. In: *ApJ* 147 (January 1967), p. 73. DOI: 10.1086/148982.

[15] Howard Baer et al. Dark matter production in the early Universe: Beyond the thermal WIMP paradigm. In: *Physics Reports* 555 (February 2015), pp. 1–60. ISSN: 0370-1573. DOI: 10.1016/j.physrep.2014.10.002.

[16] Marco Battaglieri et al. US Cosmic Visions: New Ideas in Dark Matter 2017: Community Report. 2017.

[17] Scott W. Randall et al. Constraints on the Self-Interaction Cross Section of Dark Matter from Numerical Simulations of the Merging Galaxy Cluster 1E 0657–56. In: *The Astrophysical Journal* 679.2 (June 2008), p. 1173. DOI: 10.1086/587859.

[18] Katherine Garrett and Gintaras Duda. Dark Matter: A Primer. In: *Advances in Astronomy* 2011 (December 2010), p. 968283. ISSN: 1687-7969. DOI: 10.1155/2011/968283.

[19] Jan Hamann and Jasper Hasenkamp. A new life for sterile neutrinos: resolving inconsistencies using hot dark matter. In: *Journal of Cosmology and Astroparticle Physics* 2013.10 (October 2013), p. 044. DOI: 10.1088/1475-7516/2013/10/044.

[20] Marc Kamionkowski. WIMP and Axion Dark Matter. 1997.

[21] Alexander Bähr et al. DEPFET detectors for direct detection of MeV Dark Matter particles. In: (2017).

[22] M. Cassé and P. Fayet. Light Dark Matter. In: *EAS Publications Series* 20 (2006), pp. 201–208. ISSN: 1638-1963. DOI: 10.1051/eas:2006072.

[23] Alexander Fuß. A Simulation based Neutron Background Studies for the CRESST and COSINUS Dark Matter Search Experiments. PhD thesis. Technischen Universität Wien, 2022.

[24] G. Angloher et al. The COSINUS project: perspectives of a NaI scintillating calorimeter for dark matter search. In: *The European Physical Journal C* 76.8 (August 2016), p. 441. ISSN: 1434-6052. DOI: 10.1140/epjc/s10052-016-4278-3.

[25] Jingke Xu, P.S. Barbeau, and Ziqing Hong. Detection and Calibration of Low-Energy Nuclear Recoils for Dark Matter and Neutrino Scattering Experiments. In: *Annual Review of Nuclear and Particle Science* 73.1 (2023), pp. 95–121. DOI: 10.1146/annurev-nucl-111722-025122.

[26] G. Angloher et al. Results on sub-GeV dark matter from a 10 eV threshold CRESST-III silicon detector. In: *Physical Review D* 107.12 (June 2023). ISSN: 2470-0029. DOI: 10.1103/physrevd.107.122003.

[27] Rouven Essig et al. Direct Detection of sub-GeV Dark Matter with Semiconductor Targets. 2016.

[28] Thomas Lauf. Analysis and Operation of DePFET X-ray Imaging Detectors. PhD thesis. Technische Universität München, 2011.

[29] Office of CTO. Semiconductor Devices and Process Technology. URL: http://lampx.tugraz.at/~hadley/semi/books/MKSHandBook.pdf.

[30] Emilio Gatti and Pavel Rehak. Semiconductor drift chamber — An application of a novel charge transport scheme. In: *Nuclear Instruments and Methods in Physics Research* 225.3 (1984), pp. 608–614. ISSN: 0167-5087. DOI: 10.1016/0167-5087(84)90113-3.

[31] Peter Lechner et al. Silicon drift detectors for high resolution room temperature X-ray spectroscopy. In: *Nucl. Instrum. Methods Phys. Res.* 377.2 (1996). Proceedings of the Seventh European Symposium on Semiconductor, pp. 346–351. ISSN: 0168-9002. DOI: 10.1016/0168-9002(96)00210-0.

[32] Gerhard Lutz et al. The DEPFET Sensor-Amplifier Structure: A Method to Beat 1/f Noise and Reach Sub-Electron Noise in Pixel Detectors. In: *Sensors* 16.5 (2016). ISSN: 1424-8220. DOI: 10.3390/s16050608.

[33] W. Treberspurg et al. Characterization of a 256 × 256 pixel DEPFET detector for the WFI of Athena. In: *Nucl. Instrum. Methods Phys. Res.* 958 (2020). Proceedings of the Vienna Conference on Instrumentation 2019, p. 162555. ISSN: 0168-9002. DOI: 10.1016/j.nima.2019.162555.

[34] Adrian Sorin Niculae. Development of a low noise analog readout for a DEPFET pixel detector. PhD thesis. Universität Siegen, 2003.

[35] Peter Fischer. Switcher-S, a HV Switch ASIC for DEPFET Matrix Control. Version 3.2. STZ Microelectronics & Sensor Systems. 2010.

[36] Matteo Porro, Sabine Ott, and Sebastian Albrecht. VERITAS 2.1 Data Sheet. Version : Preliminary. Max Planck-Institut für extraterrestrische Physik. 24th February 2015.

[37] H. Kluck et al. DANAE: A new effort to directly search for dark matter with DEPFET-RNDR detectors. In: *Nucl. Instrum. Methods Phys. Res.* 958 (2020). Proceedings of the Vienna Conference on Instrumentation 2019, p. 162155. ISSN: 0168-9002. DOI: 10.1016/j.nima.2019.04.109.

[38] MPG HLL Profile. URL: https://www.hll.mpg.de/3050886/HLL-Profile (visited on 21. 02. 2024).

[39] ROOT: analyzing petabytes of data, scientifically. URL: https://root.cern/ (visited on 20. 02. 2024).

[40] Jakub Kaizer, Stefano Nisi, and Pavel P. Povinec. Radiopurity measurements of aluminum, copper and selenium materials for underground experiments and mass spectrometry development. In: *Journal of Radioanalytical and Nuclear Chemistry* 322.3 (December 2019), pp. 1447–1454. ISSN: 1588-2780. DOI: 10.1007/s10967-019-06857-3.